Check for updates

ChemElectroChem

Chemistry Europe
European Chemical Societies Publishing

ChemElectroChem

RESEARCH ARTICLE OPEN ACCESS

New Polymeric Binders for the Preparation and Optimization of Pt/C-Based Electrodes for Proton-Exchange Membrane Fuel Cells (PEMFCs)

Christian Dall'Occo[1,2] | Piercarlo Mustarelli[1] | Alberto Marelli[2] | Daniele Facchi[2] | Carlo Santoro[1] | Lucia Mazzapioda[2]

[1]Department of Materials Science, University of Milano-Bicocca, Milan, Italy | [2]Syensqo Specialty Polymers Italy S.p.A., Milan, Italy

Correspondence: Carlo Santoro (carlo.santoro@unimib.it) | Lucia Mazzapioda (lucia.mazzapioda@syensqo.com)

Received: 10 May 2026 | **Revised:** 20 July 2026 | **Accepted:** 22 July 2026

Keywords: catalyst layer | ionomer | oxygen reduction reaction | PEM fuel cells

ABSTRACT

Polymeric ionomers are essential to the catalyst layer (CL) of proton-exchange membrane fuel cells (PEMFCs). This study compares two ionomers: the short-side-chain (SSC) N+125D and a high-oxygen-permeability experimental ionomer grade (EIG), the latter intended to enhance oxygen mass transport and the oxygen reduction reaction (ORR). The research evaluates ionomer–solvent interactions across various water/1-propanol mixtures to ensure structural integrity and homogeneous distribution of the electrocatalyst. Multiple ink formulations were analyzed using advanced physical–chemical characterization to determine stability and quality. These insights guided the optimization of the electrode's microstructure for integration into membrane electrode assemblies (MEAs). By employing a multidisciplinary approach, the study correlates ink formulation and electrode morphology with electrochemical performance. This integrated methodology provides a robust framework for optimizing next-generation PEMFC electrodes through a deeper understanding of ionomer behavior and structural influence within the CL.

1 | Introduction

Proton-exchange membrane fuel cells (PEMFCs) are leading low-temperature (<100 °C) electrochemical energy converters for automotive propulsion [1–3]. The core polymer electrolyte membrane (PEM)—typically a perfluorinated sulfonic acid (PFSA) ionomer—selectively conducts hydronium ions (H_3O^+) while maintaining electronic insulation and preventing reactant crossover [4, 5]. Electrochemical conversion is localized within the composite catalyst layers (CLs). At the anode, carbon-supported platinum (Pt/C) catalyzes the rapid hydrogen oxidation reaction (HOR) [6, 7]. Conversely, the cathode governs the kinetically sluggish oxygen reduction reaction (ORR) [8, 9]. The severe activation overpotential of the ORR serves as the primary thermodynamic bottleneck limiting overall PEMFC power density [1]. Consequently, current electrocatalysis research focuses on carbon-supported platinum–alloy nanoparticles (Pt-M/C, where M = Ru, Co, Ni) to optimize oxygen-binding energy, accelerate ORR kinetics, and minimize noble metal loading [10–12].

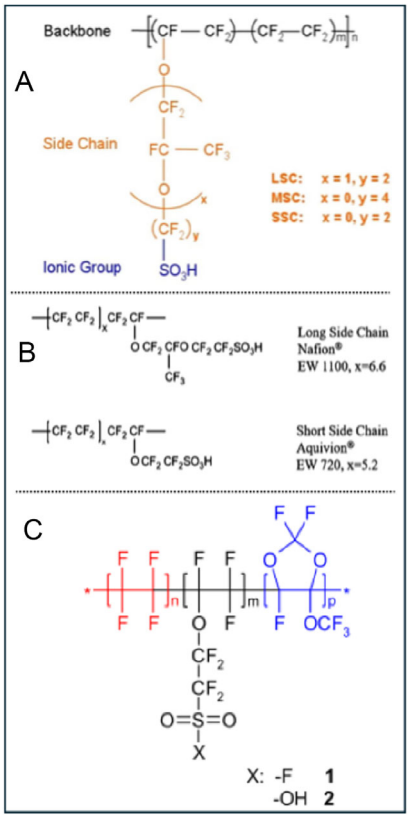
The core of a PEMFC is the membrane electrode assembly (MEA), which consists of a solid-state PEM symmetrically laminated with CLs and gas diffusion layers (GDLs). The porous, nanostructured anode and cathode CLs (5–15 μm) are deposited directly onto the PEM faces [13–15]. They consist of platinum nanoparticles supported on carbon black (Pt/C) electrocatalysts and an ionomer binder (e.g., perfluorosulfonic acid or PFSA). This configuration establishes the essential three-phase boundary (TPB), where the electronic pathway (carbon support), protonic pathway (ionomer), and fluidic channels (pores delivering H_2/O_2) intersect to sustain electrochemical reactions [16, 17]. The CLs are coupled to the GDLs, which feature a dual-layer architecture: a macroporous carbon–fiber substrate (100–300 μm) and a microporous layer (MPL) (10–50 μm) made of a carbon

This is an open access article under the terms of the Creative Commons Attribution License, which permits use, distribution and reproduction in any medium, provided the original work is properly cited.

© 2026 The Author(s). *ChemElectroChem* published by Wiley-VCH GmbH.

black–fluoropolymer composite at the CL interface. The GDL optimizes reactant gas diffusion and governs multiphase water management, preventing electrode flooding by expelling excess water while maintaining PEM humidification [18, 19]. Within the catalyst matrix, the localized ionomer network serves three functions: a structural binder securing the Pt/C particles and adhering the CL to the PEM, a proton-conducting network establishing continuous ionic pathways for H^+ transport, and a gas- permeation barrier controlling local mass transport resistance as reactants diffuse through the film to reach catalytic Pt sites [20–22].

State-of-the-art ionomers utilize PFSA copolymers with a highly phase-segregated morphology: (i) hydrophobic backbone: a polytetrafluoroethylene (PTFE)-like matrix imparting chemical resistance, thermal stability, and mechanical strength; (ii) ether-linked side chains: pendant groups whose length and spacing dictate the polymer's equivalent weight (EW). This parameter directly influences the glass transition temperature (T_g), mechanical stability, and microphase segregation [23–25]; and (iii) hydrophilic termini: acidic sulfonic acid groups (—SO_3H) that dissociate upon hydration, forming interconnected aqueous domains that facilitate rapid proton transport via Grotthuss (hopping) and vehicle (hydronium diffusion) mechanisms [23, 24]. A general structure of the PFAS is shown in Scheme 1A.



SCHEME 1 | (A) Generic structure of PFSA ionomers [24]. (B) Different side-chain length for Nafion and Aquivion [25]. (C) Example of the general structure of experimental ionomer grades (EIG). Scheme 1 was rearranged from ref. [25] with permission from the American Chemical Society, Copyright 2022.

Equivalent weight (EW, g mol^{-1} —SO_3H) dictates PFSA ionomer properties. Lowering EW increases sulfonic acid site density, enhancing proton conductivity (σ) via greater charge-carrier concentration, but increases hydrophilicity—causing excessive water uptake, dimensional swelling, and mechanical degradation. High-EW ionomers offer superior mechanical stability but lower σ. Thus, EW optimization is critical for balancing proton transport and mechanical durability, particularly in CLs where low-EW ionomers enhance Pt/C–ionomer interactions and high-current-density performance [25–27]. Nafion and Aquivion are the benchmark PFSA ionomers for PEMFCs [28–31]. Nafion features a long-side-chain (LSC) architecture (EW ≈ 1100 g mol^{-1}), balancing ionic conductivity and durability under fully humidified conditions [1, 32]. However, it suffers severe transport limitations under low relative humidity (RH) or elevated temperatures due to dehydration [33, 34]. Conversely, Aquivion employs a short-side-chain (SSC) structure with lower EW (790–980 g mol^{-1}) (Scheme 1B), yielding denser proton-conductive domains that sustain high conductivity under dehydrated or high-current-density operation [32].

Aquivion's stiffer backbone and higher crystallinity enhance mechanical and dimensional stability—even in thin-film configurations—and elevate the glass transition temperature (T_g) to ≈140 °C. This enables higher-temperature, low-RH PEMFC operation while maintaining water retention [32]. As the ORR is rate-limiting, CL design must optimize the TPB to facilitate mass transport and mitigate electrode flooding [35, 36]. The TPB comprises the electrocatalyst (Pt/C), ionic conductor (ionomer), and gaseous reactants (O_2 or H_2). Consequently, ionomer thin-film (IL) morphology and spatial distribution are critical; the IL must uniformly encapsulate the electrocatalyst particles to balance proton transport and gas diffusion [37, 38]. Excessive IL thickness introduces local oxygen-transport resistance (R_{O_2}), whereas discontinuous or ultra-thin ILs cause severe ohmic proton-transport limitations. This balance is governed by ink formulation, fabrication processes, and ionomer characteristics (architecture and EW). For instance, low-EW ionomers boost local proton conductivity but exhibit excessive swelling that triggers water flooding, blocking gas-transport pathways. Furthermore, specific adsorption of sulfonic acid (—SO_3—) groups onto Pt active sites poisons the electrocatalyst, altering its electronic environment and hindering ORR kinetics. State-of-the-art CL designs focus on maximizing the electrochemically active surface area (ECSA) and minimizing local R_{O_2}, particularly under high-current-density or dry operating conditions [35–38].

Within the CL, the ionomer-to-carbon (I/C) mass ratio is a primary parameter governing charge and mass transport. Suboptimal I/C ratios yield insufficient electrocatalyst coverage, isolating active sites due to proton-transport limitations and decreasing platinum utilization. Conversely, excessive I/C ratios lead to thick ionomer films that block the porous carbon network, exponentially increasing local R_{O_2} and promoting electrode flooding [39, 40]. Beyond the nominal I/C ratio, performance is highly sensitive to the nanoscale distribution and interfacial interactions of the ionomer with the Pt/C phase [39, 40]. Consequently, catalyst ink formulation—specifically solvent polarity and dielectric properties—is critical to achieving colloidal stability. Preventing severe Pt/C agglomeration in the liquid phase maximizes the accessible ECSA in the solid

21960216, 2026, 16, Downloaded from https://chemistry-europe.onlinelibrary.wiley.com/doi/10.1002/celc.70287 by Carlo Santoro - Area Sistemi Dipart & Doc , Wiley Online Library on [28/10/2026]. See the Terms and Conditions (https://onlinelibrary.wiley.com/terms-and-conditions) on Wiley Online Library for rules of use; OA articles are governed by the applicable Creative Commons License

state [41]. Ink rheology dictates the final CL morphology. Tailoring the shear viscosity and viscoelastic properties of the ink suppresses phase separation, flocculation, and particle coalescence. This rheological control prevents mud-cracking during drying, ensuring a mechanically cohesive film. Thus, solvent selection and dispersion media ratios are leverage points to control ink microstructure, rheological stability, and subsequent CL homogeneity [40–42]. Ultimately, CL engineering requires a holistic design framework. Balancing ionomer molecular architecture (EW), I/C ratio, interfacial thin-film morphology, and ink-colloid rheology is essential to optimize both the power density and operational lifetime of the PEMFC [41–43].

The ORR ideally proceeds via a direct four-electron ($4e^-$) pathway; however, a parasitic, less efficient two-electron ($2e^-$) pathway yielding hydrogen peroxide (H_2O_2) can occur. Mitigating this $2e^-$ pathway typically requires high platinum group metal (PGM) loadings, which substantially increases PEMFC stack costs [44, 45]. Compounding this, mass- transport kinetics are hindered by local R_{O_2} within the CL. Because conventional PFSA ionomers exhibit low oxygen permeability and form dense mass-transport barriers over the Pt/C active sites, engineering the electrocatalyst–ionomer interface to enhance local O_2 flux is critical [20, 46, 47]. Recent paradigms focus on synthesizing high-oxygen-permeability ionomers (HOPIs) to alleviate these transport bottlenecks [48, 49]. A primary strategy incorporates bulky, amorphous ring-structured monomers—such as perfluoro-(2,2-dimethyl-1,3-dioxole) (PDD)—into the PFSA backbone. The rigid, nonplanar cyclic structures prevent tight chain packing, increasing the fractional free volume (FFV) and boosting gas diffusivity [50, 51]. The general chemical architecture of these experimental ionomer grades (EIG) is shown in Scheme 1C. In the CL, HOPIs form ultra-thin, highly permeable interfacial films that lower local R_{O_2} while maintaining high proton conductivity (σ) (Figure S1) [52]. This study investigates new ink formulations for PEMFC cathode fabrication utilizing two structurally distinct ionomers: a commercially available SSC PFSA (N+125D 251/612) and a proprietary, high-oxygen-permeability polymer named EIG that is not commercially available. We evaluated various solvent-dispersion systems to optimize colloidal stability, ink rheology, and the resulting solid-state microstructural homogeneity of the electrode. Comprehensive physicochemical characterization of the liquid inks was correlated with structural and compositional analyses of the fabricated CLs. Finally, the electrodes were integrated into MEAs for in situ electrochemical evaluation. This holistic approach establishes clear structure–processing–property–performance relationships, correlating ink-colloidal properties and electrode morphology with FC polarization behavior to guide next-generation PEMFC cathode optimization.

2 | Materials and Methods

2.1 | Electrode Preparation

2.1.1 | *Electrode Fabrication and Ink Formulation*

The CL was fabricated via the colloidal dispersion and subsequent deposition of an electrocatalyst ink containing the active phase (Pt/C), an aqueous ionomer dispersion, and a binary solvent mixture. Solvent evaporation during drying yields a defined, porous transport network. The electrocatalyst employed was a commercial Pt/C (TEC10V50E, Tanaka Kikinzoku Kogyo K.K.), consisting of Pt nanoparticles (10–12 nm) supported on Vulcan XC-72R carbon (47 wt% Pt).

CLs were cast from low-boiling solvent mixtures of water (H_2O) and 1-propanol (1-PrOH), comparing two polymeric binders: commercial SSC N+125D 251/612 and experimental EIG. Formulations were adjusted to optimize (i) spatial homogeneity of the electrocatalyst, (ii) interfacial Pt/C–ionomer electronic/ionic coupling, and (iii) pore network distribution while mitigating mud-cracking. Mechanical press tests evaluated whether microcracks (which restrict the ECSA and accelerate MEA degradation) consolidated during the high-pressure hot-pressing step of MEA lamination.

To isolate the impact of ionomer architecture, the ionomer-to-carbon (I/C) ratio was fixed at 0.54, and the platinum loading was targeted at 0.3 $mg_{Pt}\,cm^{-2}$ (quantified via X-ray fluorescence, XRF). Conversely, the H_2O/1-PrOH mass ratio was varied to regulate ink rheology and colloidal stability. This was highly critical for the N+125D system, where ionomer swelling in alcohol-rich phases increases shear viscosity. The fabrication process (Figure S2) initiated with wetting the dry Pt/C with a minimum threshold volume of H_2O, followed by a 15-min ball-milling premix (MM500 Nano ball mill, zirconia media, 8 Hz) to mitigate pyrophoric ignition. Separately, the ionomer solution was prepared via magnetic stirring (500 rpm, 2 h) to achieve a total solid content (TSC) of 5 wt%, verified gravimetrically using a Mettler Toledo HX204 thermogravimetric balance. The wetted catalyst and ionomer dispersion were then co-milled (8 Hz, 2 h) to deagglomerate the carbon support and promote uniform ionomer adsorption. The ink was wet-cast onto a glass-fiber-reinforced PTFE decal substrate using a BYK BYKO-DRIVE XL doctor blade at 3 $mm\,s^{-1}$. Solvent evaporation was carried out in a ventilated oven under vacuum, utilizing a controlled thermal ramp from 40 to 100 °C at 1 °C min^{-1}. This gradual ramp suppressed capillary-force-driven cracking. Fabricated decals were sealed under inert conditions prior to testing.

2.1.2 | *MEA Integration via Decal Transfer*

MEAs were integrated using the decal transfer method. The electrodes and a reinforced Aquivion membrane (720 $g\,mol^{-1}$ EW) were laser-cut to 25 cm^2 active areas. The membrane was sandwiched between the anode and cathode decals, placed between silicone cushioning pads, and hot-pressed at 160 °C and 20 bar. Following cooling to room temperature, the PTFE backing decals were peeled off and weighed gravimetrically to determine the net transferred platinum loading (L_{Pt}).

2.2 | Physics–Chemical Characterization

2.2.1 | *Micro-XRF*

Bruker Nano GmbH micro-XRF M4 Tornado was employed to analyze the structure of the electrodes; evaluate the homogeneity of elements such as platinum, calcium and sulfur; and estimate

21960216, 2026, 16, Downloaded from https://chemistry-europe.onlinelibrary.wiley.com/doi/10.1002/celc.70287 by Carlo Santoro - Area Sistemi Dipart & Doc , Wiley Online Library on [28/10/2026]. See the Terms and Conditions (https://onlinelibrary.wiley.com/terms-and-conditions) on Wiley Online Library for rules of use; OA articles are governed by the applicable Creative Commons License

the platinum loading. Area analysis allowed to identify the distribution of elements within a defined sample region and yields two main outputs: the spectrum and the element-distribution map. Pixel dimensions below 20 µm were used to create high-resolution maps, while larger pixels above 100 µm were employed for preliminary measurements.

2.2.2 | *Digital Optical Microscope*

Digital optical microscopy provides an initial overview of the material macrostructure. Keyence VHX-7000 Series digital optical microscope was employed to acquire high-resolution images using both reflected and transmitted light-enabling rapid and nondestructive evaluation of surface features such as cracks, voids, or large inclusions. Observations were carried out in bright-field and dark-field modes to enhance contrast and highlight subtle structural details.

2.2.3 | *Dynamic Light Scattering*

Dynamic light scattering (DLS) analyses were performed using a Malvern ZS Explorer, in accordance with the normative ISO 22412 standard. DLS was employed to determine the hydrodynamic radius, zeta potential, and polydispersity index (PDI) of the samples. Multiple measurements were conducted for each sample, enabling the calculation of the standard deviation and assessment of measurement reproducibility.

2.2.4 | *Rheological Analyses*

Viscosity is a key parameter when formulating an electrode ink, and it needs to be fully balanced to ensure uniform application to the substrate. Ink viscosity needs to be (i) not too high (spreading hindering), (ii) nor too low (negative homogeneity and stability of the film). The rheometer was used for studying the rheological properties of materials, measuring the relationship between the applied shear stress and the response in terms of deformation and flow.

Specifically, an RFS III rheometer in a flat-cone configuration with a diameter of 25 mm was used. The analysis was performed by examining the rheological behavior of the ink over a shear rate range from 0 to 300 s^{-1}, while maintaining the thermostat temperature at 25 °C. In addition to viscosity of the ink, the swelling properties of the ionomers in the solvents were investigated to optimize the overall suspension viscosity since ionomer–solvent interactions play a crucial role in determining the stability of the ink.

Rheological measurements were conducted using a Rheolab QC rotational rheometer (Anton Paar) equipped with a double-gap geometry. Each 5 mL sample was analyzed using a programmable protocol set on the instrument. Two types of measurement were performed for each sample: a shear rate sweep from 0 to 1000 s^{-1} and 10 measurements at a fixed shear rate of 100 s^{-1}. Viscosity was evaluated at 100 s^{-1} because the shear stress under these conditions corresponds to that experienced during film application using the film coater. The temperature was precisely controlled throughout all measurements using the instrument's Peltier system and maintained at 25 °C.

2.2.5 | *LUMIsizer*

The LUMiSizer analytical photocentrifuge (LUM 650 dispersion analyzer GmbH) is a cuvette-based centrifuge that operates using STEP-technology. The instrument was used to study the kinetic stability of the inks, with a particular focus on determining their clarification rate. Kinetic stability is used for evaluating the colloidal properties of inks because it describes the resistance to phase-separation processes arising from aggregation, flocculation, and sedimentation [53]. Experimentally, the analyses were carried out by diluting the sample in vial (10 mm OD) with 1 mL of solvent. The transmitted light was monitored by scanning the entire sample volume for 35 h at 25 °C. Measurements were performed using the 870 nm light source during centrifugation at 32 g-force.

2.3 | Electrochemical Characterization

The in-cell characterization was performed using a series of standardized tests aimed at evaluating the overall PEMFC performance. These tests were carried out at Syensqo Lab in Bollate, Milan, Italy.

2.3.1 | *Cyclic Voltammetry (CV) Studies*

CV is used in PEMFC studies to evaluate the ECSA, which is a key parameter that reflects the number of effective active sites in the CL. The ECSA can be calculated using the following equation (Equation (1)):

$$\mathrm{ECSA}\left(\frac{\mathrm{cm^2Pt}}{\mathrm{gPt}}\right) = \frac{Q\left(\frac{\mu C}{cm^2}\right)}{210\left(\frac{\mu C}{cm^2 Pt}\right) \times \text{catalyst loading}\left(\frac{g_{Pt}}{cm^2}\right)} \quad (1)$$

Q is the charge obtained by integrating the hydrogen adsorption/desorption peaks during the CV. The value of 210 µC cm^{-2} Pt represents the charge associated with hydrogen adsorption on a smooth platinum electrode, while the electrocatalyst loading corresponds to the total number of reactive surface sites in the CL. The integration excludes the contribution from the double-layer charging/discharging. During the experiment, the reference electrode was subjected to a triangular voltage sweep within a potential range where the charge transfer is governed by the hydrogen adsorption/desorption reactions at the active sites. The measured charge density is then used to calculate the roughness factor (r.f., $cm^2\ cm^{-2}$), which represents the active surface area of the catalyst per unit of geometric electrode area, and the ECSA ($cm^2\ mg^{-1}$), defined as the active catalyst surface area per unit mass of electrocatalyst.

The test was conducted at 100% RH and 30 °C, using the following parameters:

- Anode mass flow: 1 NLPM H_2,
- Cathode mass flow: 0.1 NLPM N_2,
- Temp. anode endplate: 30 °C,
- Temp. anode inlet = Temp. cathode inlet = 35 °C, and
- Temp. bipolar plates anode = Temp. Bipolar plates cathode = 30 °C.

21960216, 2026, 16, Downloaded from https://chemistry-europe.onlinelibrary.wiley.com/doi/10.1002/celc.70287 by Carlo Santoro - Area Sistemi Dipart & Doc , Wiley Online Library on [28/10/2026]. See the Terms and Conditions (https://onlinelibrary.wiley.com/terms-and-conditions) on Wiley Online Library for rules of use; OA articles are governed by the applicable Creative Commons License

2.3.2 | Polarization Curve

Polarization curves were measured at 80 °C and at RH of 35%, 65%, and 100% [53]. The measurements were performed with H_2/air feeds at the anode and cathode, under operating pressures of 50 kPa (anode, relative) and 50 kPa (cathode, relative), using mass-flow stoichiometries as follows: For current densities above 0.2 A cm^{-2}, a fixed stoichiometric ratio was applied; for lower current densities, a fixed flow rate was maintained, corresponding to the flow at 0.2 A cm^{-2}.

2.3.3 | Electrochemical Impedance Spectroscopy (EIS)

The following protocol outlines the method used to measure EIS, which assesses the kinetics and mass-transport impedance under operational conditions:

- Anode endplate temperature: 80 °C (cell temperature),
- Anode inlet temperature: 85 °C,
- Cathode inlet temperature: 85 °C,
- Anode inlet pressure: 50 kPa (gauge), and
- Cathode inlet pressure: 50 kPa (gauge).

The tests were carried out at three different RH levels: 35%, 65%, and 100%. The corresponding dew-point temperatures (T_DP) for the anode and cathode saturators were set as follows to achieve the desired RH values:

- 35% RH: T_DP anode = T_DP cathode = 56.1 °C
- 65% RH: T_DP anode = T_DP cathode = 69.7 °C
- 100% RH: T_DP anode = T_DP cathode = 80.0 °C.

Between different humidity conditions, the cell was conditioned for 1 h under H_2/N_2 flows (0.45 NLPM/1.1 NLPM, respectively) prior to testing to ensure proper MEA stabilization. EIS measurements were performed at low and high current densities, specifically 0.02 and 0.8 A cm^{-2}. Gas flows were set to maintain a stoichiometric ratio of 1.5/2 H_2/air at high current density, while at low current density, the flows were calculated to achieve the same stoichiometric ratio at 0.2 A cm^{-2}.

The specific mass flows used for EIS measurements were as follows:

- $i = 0.02$ A cm^{-2}:
  - Anode mass flow = 0.048 NLPM
  - Cathode mass flow = 0.15 NLPM
- $i = 0.8$ A cm^{-2}:
  - Anode mass flow = 0.19 NLPM
  - Cathode mass flow = 0.61 NLPM.

The protocol for measuring ion-transport resistance under equilibrium conditions is detailed here:

- Anode endplate temperature: 80 °C (cell temperature),
- Anode inlet temperature: 85 °C,
- Cathode inlet temperature: 85 °C, and
- No back pressure applied.

The tests were carried out at four different RH levels: 30%, 50%, 90% and 100%. Between different humidity conditions, 1-h period is waited to allow cell conditioning.

2.3.4 | Limiting Current Measurements

Limiting current measurement is a well-established method for evaluating mass-transport resistance in PEMFCs. The limiting current is defined as the maximum current density at which the oxygen concentration at the cathode electrocatalyst interface approaches 0, which corresponds to the mass-transport region of the polarization curve. The corresponding oxygen-transport resistance can be calculated as follows:

$$R_{\mathrm{MT}} = \frac{\Delta C}{N_{\mathrm{O_2}}} = 4F\frac{\Delta C}{i}$$

where ΔC is the concentration difference between oxygen in the gas channel ($C_{\mathrm{O_2GC}}$) and oxygen at the electrocatalyst interface, is the oxygen flux, and R_{MT} is the total mass transport resistance. Under limiting current conditions, the oxygen concentration at the Pt interface tends to 0, and therefore the total mass transport resistance can be expressed as follows:

$$R_{\mathrm{MT}} = 4F\frac{C_{\mathrm{O_2GC}}}{i_{\mathrm{lim}}} = \frac{4F\chi_{\mathrm{O_2}}^{\mathrm{in,dry}}}{i_{\mathrm{lim}}}\frac{p - p_{\mathrm{w}}}{RT}$$

where p is the total cathode pressure, p_{W} is the water-vapor partial pressure, and $\chi_{\mathrm{O_2}}^{\mathrm{in,dry}}$ is the dry oxygen mole fraction at the cathode inlet. R_{MT} represents the combined contribution of multiple transport resistances within the cell. These can be grouped into two categories: pressure-dependent resistances, associated with intermolecular diffusion through the gas channel, GDL and MPL up to the CL interface; and pressure-independent resistances, associated with Knudsen diffusion and diffusion through liquid water or the ionomer film at the Pt interface [54, 55] as schematized in Figure S3.

The tests were performed under the following operating conditions:

- Cooling temperature: 80 °C,
- Cooling gas flow: 0.5 NLPM,
- Dew-point temperature (T_DP) for anode and cathode: 69.7 °C (corresponding to 65% RH),
- Anode and cathode gas inlet temperatures: 85 °C,
- Anode mass flow: 0.65 NLPM (H_2), and
- Cathode mass flow: 2 NLPM (O_2/N_2 mixture).

The limiting current was determined by performing a voltage scan from 0.3 to 0.1 V, with a step of 0.02 V and a duration of 2 min per step. To remove contributions not related to

21960216, 2026, 16, Downloaded from https://chemistry-europe.onlinelibrary.wiley.com/doi/10.1002/celc.70287 by Carlo Santoro - Area Sistemi Dipart & Doc , Wiley Online Library on [28/10/2026]. See the Terms and Conditions (https://onlinelibrary.wiley.com/terms-and-conditions) on Wiley Online Library for rules of use; OA articles are governed by the applicable Creative Commons License

oxygen transport (e.g., current due to hydrogen evolution), the voltage scan was repeated at three different oxygen concentrations: 1%, 2%, and 3%. The limiting current measurements were then repeated at four different operating pressures: 50, 100, 150, and 200 kPa (gauge). The pressure was set at the cell inlet and maintained equal for both anode and cathode [56, 57].

3 | Results and Discussion

3.1 | Results Obtained From the Pt/C-Based Catalyst Inks Prepared With Ionomer N+125D 251/612

This section presents the results achieved with the polymeric binder N+125D 251/612, utilizing the ink and electrode preparation methods described in Section 2.

3.1.1 | Ionomer N+125D 251/612 Preparation

Initial ink development focused on polymer solvation dynamics in binary water/1-propanol (H_2O/1-PrOH) mixtures. Unlike water—which acts primarily as a dispersing agent—the amphiphilic structure of 1-PrOH promotes localized swelling of the perfluorinated backbone. This conformational expansion increases the hydrodynamic radius (R_h) and macroviscosity. Consequently, capillary viscometry and dynamic light scattering (DLS) were employed to quantify the resulting rheological profiles and swelling kinetics. In Table 1, the quantities used to prepare both N+125 formulations and their corresponding TSC are presented including

- Dispersion of N+125D 251/612 in water with a TSC of 25%,
- N+125D 251/612 formulated with a 50/50 (water/1-propanol) mixture and a TSC of 5%, and
- N+125D 251/612 formulated with a 25/75 (water/1-propanol) mixture and a TSC of 5%.

TABLE 1 | Materials used in the formulation using N+125D 251/612 and their corresponding TSC.

Components	N+125D 251/612-formulated 50/50 (water/1-propanol)	N+125D 251/612-formulated 25/75 (water/1-propanol)
1-Propanol, g	25.59	38.15
N+125D, g	10.00	10.00
Water, g	18.29	5.39
TSC of the formulated ionomer, w/w%	5.22	5.24
TSC dispersion of N+125D 251/612, w/w%	26.94	26.94

The relative viscosity curves for all samples using N+125D 251/612 ionomer are reported in Figure 1A.

Viscosity (η) scales positively with the 1-PrOH volume fraction. The neat N+125D 251/612 dispersion exhibits the lowest baseline viscosity and maintains shear-rate-independent Newtonian behavior. Formulations prepared with 50/50 and 25/75 H_2O/1-PrOH mass ratios likewise exhibit stable, Newtonian rheological profiles across the investigated shear-rate spectrum. This rheological shift confirms solvent-induced conformational rearrangement and steric swelling of the PFSA chains upon interaction with 1-PrOH. DLS analyses presented in Figure 1B reveal a progressive increase in the average hydrodynamic radius (R_h) of N+125D aggregates with increasing alcohol content, corroborating the macroviscosity trends and validating the chain-expansion mechanism. Concurrently, the PDI (Figure 1C) scales with 1-PrOH concentration, indicating a transition to a highly polydisperse colloidal state that exceeds the classical monodisperse limit (PDI < 0.10).

3.1.2 | Ink Formulation Including Ionomer N+125D 251/612

The ionomer dispersions formulated at 50/50 and 25/75 H_2O/1-PrOH mass ratios were utilized to prepare Pt/C electrocatalyst inks according to the protocol in Section 2.1. The quantitative compositions and measured total solid contents (TSC) are detailed in Table 2. To maintain a standardized, uniform 50/50 H_2O/1-PrOH solvent ratio in the final ink matrix, the secondary water addition during the electrocatalyst wetting step was adjusted, resulting in a higher water mass for the 25/75-derived formulation. The rheological profiles of the resulting inks were characterized to elucidate the colloidal interactions between the electrocatalyst particles and the solvated ionomer phase. Viscosity curves (Figure 2A) reveal that the Pt/C ink prepared with the 50/50 precursor dispersion exhibits a marginally higher shear viscosity than the 25/75 counterpart. This trend reverses the viscosity behavior observed in the neat ionomer dispersions, which is attributed to the dilution effect of the substantially higher water content (an 11-fold increase) added during the electrocatalyst wetting phase of the 25/75 formulation (Table 2).

To better understand this discrepancy, DLS analysis was performed on both inks. The results are presented in Figure 2B,C. Contrary to the viscosity trend, the DLS results reveal larger polymer particles for the 25/75 sample compared to the 50/50 sample. This trend aligns more closely with the previous findings [33].

The stability of both inks using the LUMIsizer and the transmittance profiles of both inks is presented in Figure 2D,E. The ink prepared with the 50/50 H_2O/1-PrOH formulation shows clarification at the top of the vial. In contrast, the other ink displays high transmittance even beyond 120 mm along the vial. Additionally, the transmittance profiles analysis reveals that both inks do not have a uniform particle distribution, being a polydisperse system, as confirmed by the DLS analysis (Figure 2C), with PDI values around 0.20 for both inks. Clarification rate graphs for both samples exhibit a comparable

21960216, 2026, 16, Downloaded from https://chemistry-europe.onlinelibrary.wiley.com/doi/10.1002/celc.70287 by Carlo Santoro - Area Sistemi Dipart & Doc , Wiley Online Library on [28/10/2026]. See the Terms and Conditions (https://onlinelibrary.wiley.com/terms-and-conditions) on Wiley Online Library for rules of use; OA articles are governed by the applicable Creative Commons License

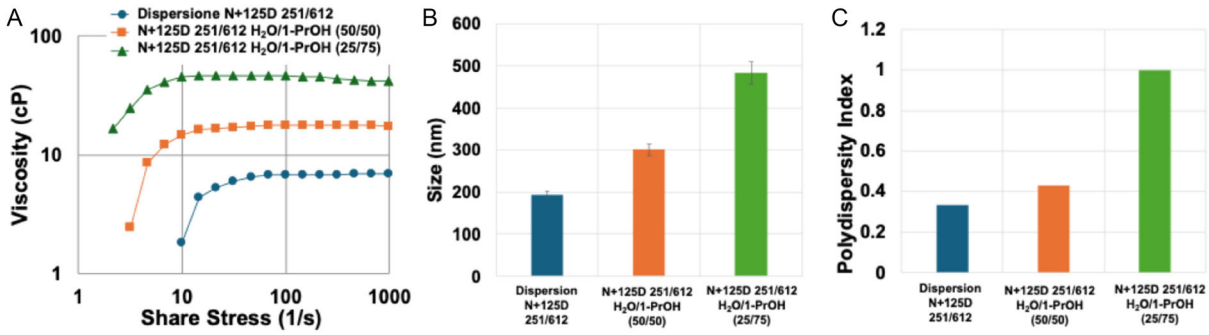


FIGURE 1 | (A) Viscosity curves for both the dispersion and the formulations prepared with N+125D 251/612. (B) and (C) Particle sizes and polydispersity index (PDI) obtained through DLS analysis data of the ionomer N+125D 251/612 formulated with different alcohols content.

TABLE 2 | Materials used in the Pt/C catalyst ink containing N+125D and their corresponding TSC.

Components	Ink (water/1-PrOH 50/50) N+125D 251/612 formulated with 50/50 (water/1-PrOH)	Ink (water/1-PrOH 50/50) N+125D 251/612 formulated with 25/75 (water/1-PrOH)
Ionomer formulated, g	11.5	11.5
Pt/C, g	2	2
Water, g	0.5	5.46
TSC ink, w/w%	16.28	11.76

rate (14.36 vs. 14.86 mm/month), suggesting similar stability over time (Figure 2F,G).

From these preliminary findings, it can be inferred that solvating the Aquivion N+125D 251/612 ionomer in alcohol-rich media promotes macromolecular aggregation, yielding larger hydrodynamic diameters (D_h) that correlate positively with the alcohol-to-water ratio. This structural trend translates directly to the multicomponent Pt/C catalyst inks, wherein the maximum average hydrodynamic particle size is exhibited by the formulation utilizing the N+125D 251/612 dispersion at a 25/75 wt% H_2O/1-PrOH ratio. Anomalous rheological behavior, however, was detected in the steady-state shear viscosity profiles. This deviation is hypothesized to stem from variations in the ink-preparation protocol. Specifically, during the synthesis of the 25/75 H_2O/1-PrOH-derived ink (targeting a nominal 50/50 H_2O/1-PrOH final solvent matrix), a significantly greater volume of deionized water was introduced postelectrocatalyst prewetting relative to the benchmark 50/50 H_2O/1-PrOH ink. For the latter, the majority of the aqueous phase was integrated during the initial dispersion formulation, with only a nominal fraction allocated for electrocatalyst prewetting (Table 2). This localized dilution effect likely altered the microstructural evolution of the ink, disrupting the transient "aging" (conformational equilibration) of the ionomer in the alcohol-rich environment. Consequently, the interfacial interactions and adsorption kinetics between the Pt/C electrocatalyst and the ionomer during high-shear mixing were perturbed. Another key distinction lies in the flow behavior of the systems. While the neat ionomer dispersion exhibits Newtonian flow (where dynamic viscosity (η) remains independent of the applied shear rate), both Pt/C-loaded inks display pronounced non-Newtonian shear-thinning (pseudoplastic) behavior. Due to the absence of transient, time-dependent rheological testing (e.g., three-step shear tests or hysteresis loop measurements), a definitive distinction between pure pseudoplasticity and thixotropy cannot be established.

To mitigate these preparation-induced discrepancies, an optimized Pt/C catalyst ink was synthesized utilizing the N+125D 251/612 dispersion at a 25/75 H_2O/1-PrOH ratio. The compounding protocol was modified by normalizing the water addition sequence to maintain identical solvent-displacement dynamics in the final composition. Specifically, the water volume introduced during the carbon prewetting phase was kept congruent with that of the 50/50 H_2O/1-PrOH baseline ink. The precise mass balances for this modified formulation are cataloged in Table S1. The newly formulated Pt/C-based ink underwent identical diagnostic characterization, including rotational rheometry and DLS analysis, as compiled in Figure 3. Figure 3A compares the steady-shear viscosity profiles of the baseline 50/50 formulation against the optimized 25/75 ink. Upon modulating the water- addition sequence for the 25/75 ionomer-based formulation, the ink exhibited a higher viscosity profile across the investigated shear-rate range. This rheological shift aligns with the intrinsic viscosity trends observed for the parent Aquivion dispersions (cf. Figure 2A).

Figure 3B illustrates the DLS volume-metric size distributions, which correlate strongly with the steady-shear rheological profiles. The colloidal dispersion formulated with the 25/75 H_2O/1-PrOH N+125D 251/612 ionomer displayed a distinct shift toward larger hydrodynamic diameters (D_h), corroborating the hypothesis of enhanced macromolecular swelling and chain extension in the presence of higher alcohol fractions. Space- and time-resolved transmittance profiles reveal nonuniform particle sedimentation, a hallmark of polydisperse colloidal systems. This is quantitatively substantiated by the DLS PDI values, which consistently exceeded 0.1—particularly for the ink synthesized with the 25/75 ionomer formulation. This indicates that an elevated alcohol fraction broadens the particle size distribution, resulting in a more heterogeneous microstructure (Figure 3C). Notably, despite its broader polydispersity, the ink prepared with

21960216, 2026, 16, Downloaded from https://chemistry-europe.onlinelibrary.wiley.com/doi/10.1002/celc.70287 by Carlo Santoro - Area Sistemi Dipart & Doc , Wiley Online Library on [28/10/2026]. See the Terms and Conditions (https://onlinelibrary.wiley.com/terms-and-conditions) on Wiley Online Library for rules of use; OA articles are governed by the applicable Creative Commons License

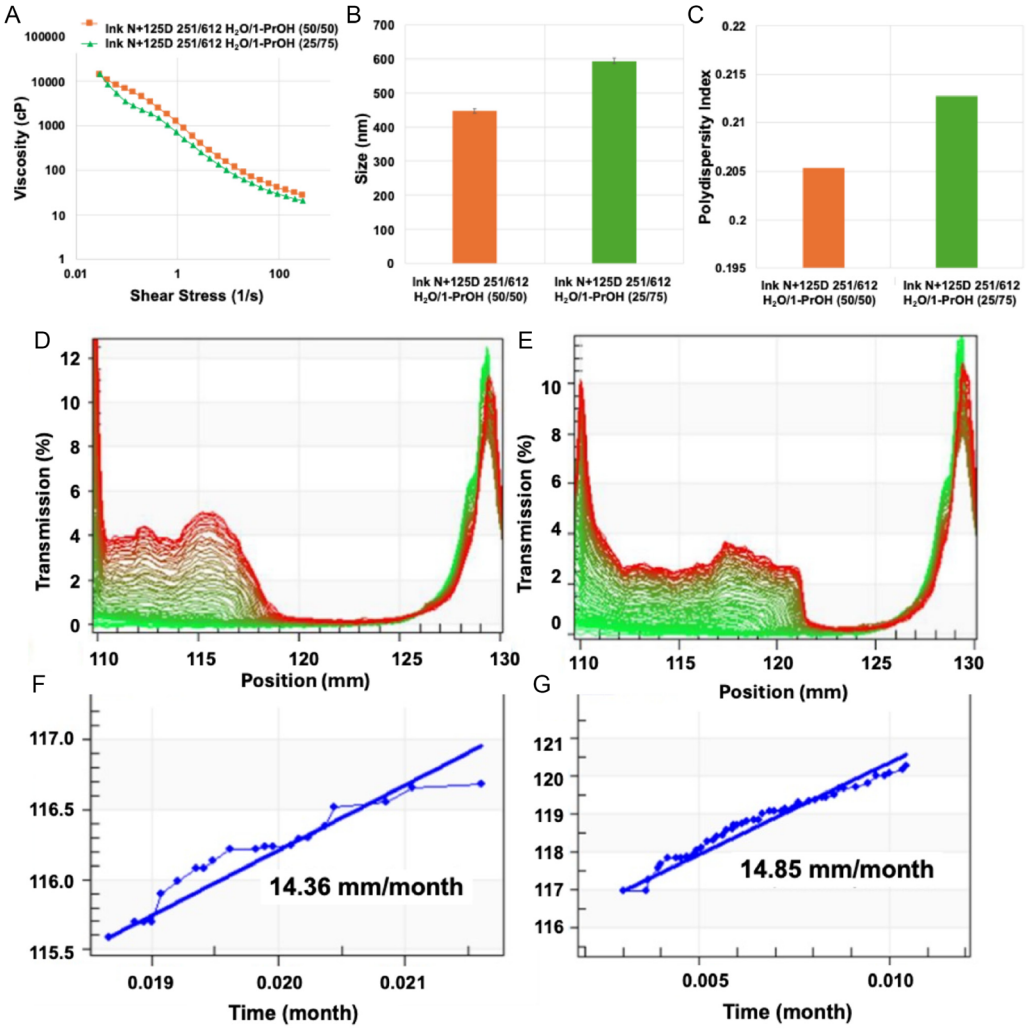


FIGURE 2 | (A) Viscosity curves of the ink prepared with N+125D 251/612 formulated with different water/1-propanol ratios. (B) and (C) Particle sizes and polydispersity index (PDI) of both inks prepared with N+125D 251/612 formulated with alcohols obtained by DLS analysis. (D) and (E) LUMIsizer analysis of both inks formulated with N+125D 251/612 at a 50/50 water/1-propanol ratio and 25/75. (F) and (G) Clarification rate graph for the ink prepared with N+125D 251/612 at a 50/50 water/1-propanol ratio and the ink prepared at a 25/75 water/1-propanol ratio.

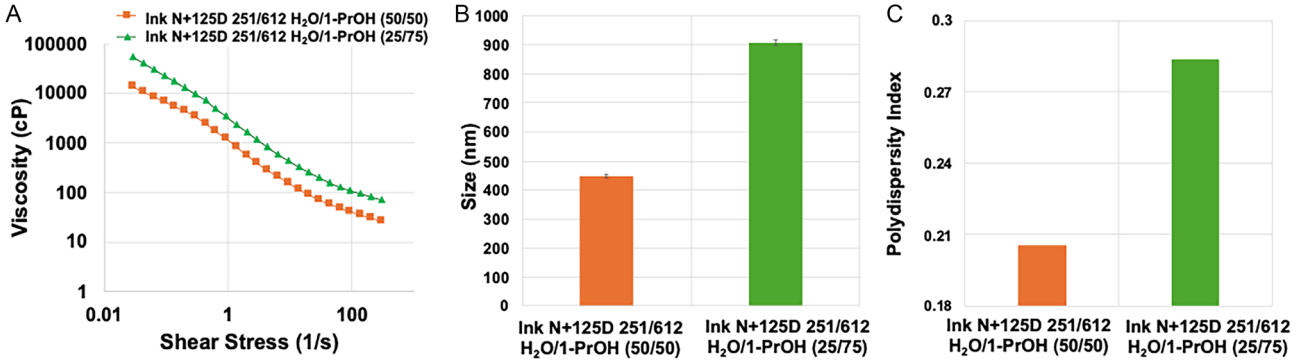


FIGURE 3 | (A) Viscosity curves of the ink prepared with N+125D 251/612 at two different water/1-propanol ratios. (B) and (C) Particle sizes and polydispersity index (PDI) of the ink with N+125D at two different water/1-propanol ratios obtained by DLS analysis.

the 25/75 H_2O/1-PrOH ratio demonstrated superior colloidal stability under accelerated gravitational fields, as evaluated by analytical centrifugation (LUMIsizer, Figure S4). This formulation exhibited negligible phase separation, rendering the determination of clarification kinetics mathematically indeterminate due to the absence of a distinct settling front.

21960216, 2026, 16, Downloaded from https://chemistry-europe.onlinelibrary.wiley.com/doi/10.1002/celc.70287 by Carlo Santoro - Area Sistemi Dipart & Doc , Wiley Online Library on [28/10/2026]. See the Terms and Conditions (https://onlinelibrary.wiley.com/terms-and-conditions) on Wiley Online Library for rules of use; OA articles are governed by the applicable Creative Commons License

3.2 | Results Obtained for the Pt/C Electrodes Prepared With N+125D 251/612

To elucidate the correlation between ink physicochemical properties and the resulting CL microstructures, electrodes were fabricated using the optimized Pt/C formulations. For comparative clarity, the electrode cast from the 50/50 H_2O/1-PrOH ink is designated as **E-1**, and the counterpart cast from the adjusted 25/75 H_2O/1-PrOH ink is designated as **E-2**. Surface morphology and defect density were initially assessed via optical microscopy at 300× magnification (Figure S5). E-1 exhibits a more heterogeneous surface topography characterized by superficial microcracks, whereas E-2 displays a more cohesive and continuous plane. Notably, neither electrode exhibits deep, penetrating mud-cracking. This indicates that the localized rheological variations and the elevated 1-propanol fraction did not critically compromise the wet-film casting or the subsequent solvent-evaporation kinetics during the drying phase. The spatial distribution of the active components was resolved quantitatively using micro-X-ray fluorescence (μ-XRF) spectroscopy (Figure 4), which illustrates the elemental mapping of platinum (Pt, representing the electrocatalyst phase) and sulfur (S, representing the sulfonic acid groups of the Aquivion ionomer) for both E-1 (Figure 4A) and E-2 (Figure 4B).The Pt map for E-1 (Figure 4A) demonstrates a highly uniform lateral distribution across the macroscale projection, yielding an average electrocatalyst loading of 0.291 mg cm^{-2}. Concurrently, the sulfur mapping confirms that the ionomer phase achieved homogeneous codispersion within the electrocatalyst matrix. In contrast, the calcium (Ca) mapping effectively traces the underlying texture of the PTFE transfer substrate. Consequently, these findings highlight that PTFE is a suboptimal decal substrate for CL fabrication; overlay analysis of the Pt, S, and Ca maps reveals that the substrate's surface roughness dictates the deposition profile of the ink, with both the ionomer and the Pt/C electrocatalyst showing a thermodynamic preference to segregate and accumulate within the topographical recesses of the PTFE mesh.

For E-2 (Figure 4B), the instrumentally determined average Pt loading is 0.233 mg cm^{-2}, falling below the nominal target specification. Furthermore, the lateral distribution of the electrocatalyst exhibits higher spatial heterogeneity relative to E-1. Superimposing the Pt, S, and Ca elemental maps reveals pronounced localized domains characterized exclusively by sulfur signals. This spatial segregation suggests suboptimal interfacial interaction and binding affinity between the sulfonic acid functionalities (—SO_3H) of the ionomer and the Pt/C electrocatalyst nanoparticles within this specific CL microstructure. Correlating these findings, the ink formulated with the 25/75 H_2O/1-PrOH ratio displays superior colloidal stability compared to the 50/50 analog. Conversely, at the electrode level, the CL derived from the 50/50 dispersion exhibits superior morphological homogeneity and elemental distribution. This discrepancy is attributed to the elevated low-shear viscosity of the 25/75 formulation, which increases hydrodynamic resistance during wet-film deposition, potentially inducing shear-induced flow instabilities. Additionally, the synergistic effects of higher viscosity and a dominant 1-propanol fraction alter the solvent evaporation rate, modifying the consolidation kinetics and potentially promoting Marangoni-type phase segregation during drying compared to the 50/50 benchmark.

4 | High-Oxygen-Permeable Ionomers EIG

In this section, the results obtained using EIG as the polymeric binder are presented. The procedure used for the preparation of the ink, the electrode, and the MEA is the same as for the other polymeric binder investigated in this study.

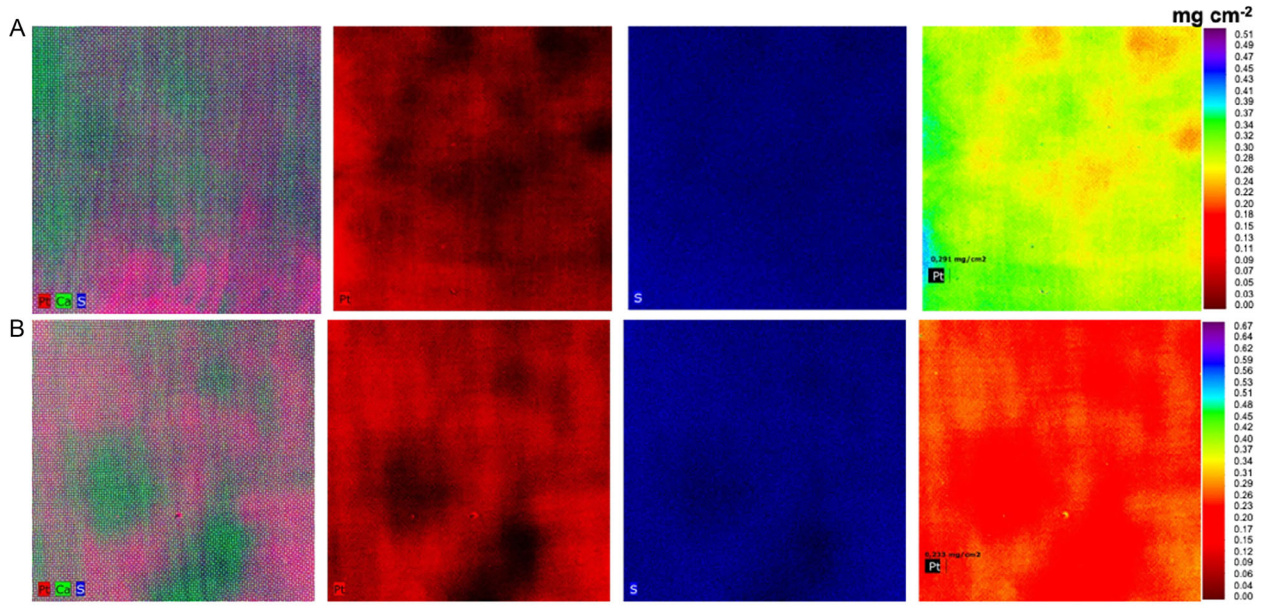


FIGURE 4 | (A) and (B) Mapping of platinum, sulfur, and calcium, and average Pt loading for electrode E-1 (0.291 mg cm^{-2}) and E-2 (0.233 mg cm^{-2}), based on micro-XRF analysis.

21960216, 2026, 16, Downloaded from https://chemistry-europe.onlinelibrary.wiley.com/doi/10.1002/celc.70287 by Carlo Santoro - Area Sistemi Dipart & Doc. , Wiley Online Library on [28/10/2026]. See the Terms and Conditions (https://onlinelibrary.wiley.com/terms-and-conditions) on Wiley Online Library for rules of use; OA articles are governed by the applicable Creative Commons License

TABLE 3 | Materials used in the formulation using EIG and their corresponding TSC.

Components	EIG-formulated 50/50 (water/1-propanol)	EIG-formulated 25/75 (water/1-propanol)
1-Propanol, g	12.13	18.19
N+125D, g	5	5
Water, g	8.40	2.34
TSC of the formulated ionomer, w/w%	5.12	5.17
TSC dispersion of EIG, w/w%	25.53	25.53

4.1 | Results Obtained From the Pt/C-Based Electrocatalyst Inks Prepared With EIG

To better understand the properties of the EIG polymer, it was also formulated with 1-propanol, using the same water/alcohol ratio as for the N+125D 251/612 dispersion. In Table 3, the weights of all components and the TSC values for both the original EIG dispersion and after formulation are reported with the polymer content was maintained at approximately 5%.

To elucidate the solvation dynamics between the EIG binder and the binary aqueous-organic media, the steady-state dynamic viscosity (η) profiles of the pristine EIG dispersion and its 1-propanol-formulated counterparts were evaluated (Figure 5A). All three systems exhibit strictly Newtonian flow behavior across the investigated shear-rate range. However, unlike the N+125D 251/612 dispersion, modulating the 1-propanol concentration yielded no statistically significant deviation in viscosity. This rheological insensitivity indicates a considerably lower swelling ratio for the EIG binder, which can be attributed either to poor thermodynamic affinity between 1-propanol and the EIG polymer backbone, or to the structurally rigid backbone conformation of EIG relative to the more flexible N+125D 251/612 macromolecular chains. Because the 25/75 H_2O/1-PrOH EIG formulation induced no appreciable viscosity increase, subsequent investigations focused exclusively on the benchmark EIG system formulated at a 50/50 wt% H_2O/1-PrOH ratio.

Accordingly, Figure 5B,C presents the DLS size distributions and PDI of the EIG dispersion in its pristine state versus the 50/50 H_2O/1-PrOH formulation. Despite the negligible change in bulk viscosity, the average hydrodynamic diameter (D_h) of the binder aggregates shifted from approximately 120 to 200 nm post-formulation, confirming a localized polymer–solvation interaction. Nevertheless, this swelling response is remarkably muted compared to the N+125D 251/612 system, where the hydrodynamic size doubled from 450 to 900 nm. Consequently, a Pt/C catalyst ink was prepared using the EIG binder formulated at the 50/50 H_2O/1-PrOH ratio. The corresponding formulation mass balances and the determined TSC are detailed in Table S2.

The steady-state rheological profile of the EIG-based Pt/C catalyst ink was evaluated and benchmarked against the previously synthesized formulations (Figure S6). The EIG 50/50 H_2O/1-PrOH and N+125D 25/75 H_2O/1-PrOH inks display nearly identical shear-viscosity profiles, whereas the baseline N+125D 251/612 50/50 formulation exhibits a significantly lower viscosity across the entire shear spectrum. DLS analysis of the EIG-containing Pt/C ink resolved an average hydrodynamic diameter

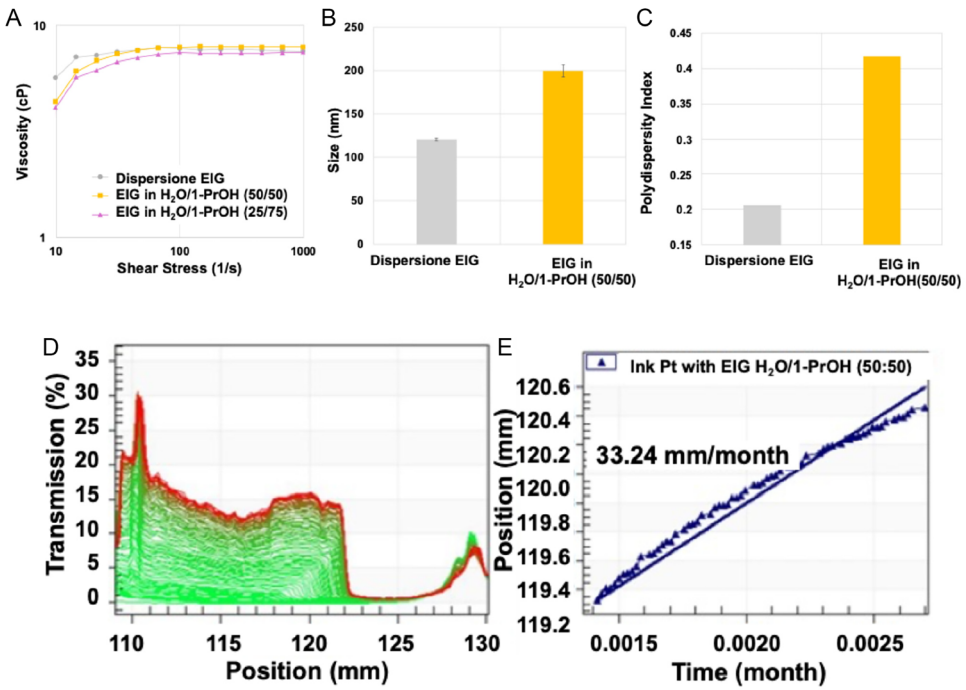


FIGURE 5 | (A) Viscosity curves of the dispersion and of the formulations prepared with EIG. (B) and (C) Particle sizes and polydispersity index (PDI) of the formulation with EIG obtained by DLS analysis. (D) and (E) LUMIsizer analysis and clarification rate graph of the ink formulated with EIG at a 50/50 water/1-propanol ratio.

21960216, 2026, 16, Downloaded from https://chemistry-europe.onlinelibrary.wiley.com/doi/10.1002/celc.70287 by Carlo Santoro - Area Sistemi Dipart & Doc , Wiley Online Library on [28/10/2026]. See the Terms and Conditions (https://onlinelibrary.wiley.com/terms-and-conditions) on Wiley Online Library for rules of use; OA articles are governed by the applicable Creative Commons License

(D_h) of 592 ± 12 nm with a corresponding PDI of 0.2871. Comparing the colloidal dimensions, the aggregate size in the EIG ink exceeds that of the N+125D 50/50 formulation ($D_h \approx 448$ nm), which directly correlates with the elevated low-shear viscosity of the EIG-based system. Conversely, the EIG-ink particle size is marginally smaller than that of the N+125D 25/75 counterpart. This subtle spatial divergence manifests at elevated shear rates, where the viscosity curve of the EIG system drops slightly below that of the N+125D 25/75 benchmark due to more pronounced shear-thinning. Accelerated sedimentation analysis via analytical centrifugation (LUMIsizer, Figure 5D) reveals parallel step-transmittance profiles spanning up to a radial position of 122.5 mm in the measurement cell. This behavior indicates a polydisperse, zone-settling consolidation mechanism. Crucially, the computed clarification velocity of the EIG formulation is significantly higher than those recorded for the N+125D-based systems, indicating accelerated phase-separation kinetics and, consequently, lower overall colloidal stability for the EIG-derived ink (Figure 5E).

4.1.1 | Results Obtained for the Pt/C Electrodes Prepared With N+125D 251/612

A Pt/C CL was fabricated using the EIG binder according to the established protocol to yield electrode **E-3**. This sample was subsequently characterized via optical microscopy and μ-XRF spectroscopy, mirroring the diagnostics applied to E-1 and E-2. Surface topographies of E-3 at 100 times and 300 times magnifications are shown in Figure S7. The micrographs reveal a highly heterogeneous surface morphology marred by substantial mechanical defects. These macrodefects consist of microcracks of varying depths; while some remain restricted to the superficial boundary layer, others penetrate through the entire CL thickness, allowing back-light transmission. The propagation of such deep, through-plane mud-cracks is highly detrimental, as they compromise the mechanical integrity of the CL, accelerate localized delamination, and degrade the ECSA. To mitigate this structural fragility, the electrode was subjected to a thermomechanical hot-pressing step under typical MEA lamination parameters (20 bar, 160 °C, $t = 5$ min) to evaluate crack healing. Figure S8 contrasts the optical morphology of the CL pre- and postlamination. Postpressing, a significant closure of the through-plane cracks and a major reduction in superficial microcracks are observed. This plastic deformation confirms that fabrication-induced macrodefects in the EIG-based CL can be successfully consolidated, restoring the mechanical continuity required for stable fuel-cell (FC) operation.

The spatial distribution of the active components and the average platinum loading of E-3 were resolved quantitatively via μ-XRF. Figure S9 displays the elemental maps for Ca, Pt, and S, alongside the calculated Pt mass loading. The μ-XRF maps demonstrate a highly uniform lateral distribution of the Pt/C electrocatalyst, although minor localized microvoids are visible, alongside a slight gradient of decreasing Pt concentration toward the lower edge of the electrode. The calculated average platinum loading is 0.323 mg cm^{-2}, which is highly congruent with the nominal target loading. Crucially, the spatial superposition of the Pt and S signals shows excellent colocalization, confirming a high thermodynamic affinity and strong interfacial interaction between the EIG binder and the Pt/C electrocatalyst phase.

5 | Electrochemical Tests and Comparisons

The performance of the MEAs prepared with the electrodes described in the previous paragraphs is presented. All electrochemical tests were conducted according to the protocols described in Section 2.

Three different MEAs were tested:

- **MEA-1** contains E-1 electrodes used as both anode and cathode.
- **MEA-2** contains E-2 electrodes used as both anode and cathode.
- **MEA-3** contains E-1 electrode used and anode and contains the E-3 electrode, prepared with the EIG binder to provide lower oxygen resistance and improve oxygen permeability through the CL, as the cathode.

5.1 | Polarization and Power Curves

The electrochemical polarization ($V-j$) and power density ($P-j$) characteristics of the three MEAs were evaluated under a gradient of RH operating conditions: 100% RH, 65% RH, and 35% RH.

Figure 6 compares the isothermal (80 °C) electrochemical response of the three MEAs under fully humidified conditions (100% RH) via polarization curves (Figure 6A) and power-density profiles (Figure 6B). All cells exhibit typical PEMFC behavior, where cell potential (V) decreases monotonically with increasing current density (j) due to cumulative overpotentials. In the activation-controlled region ($j \to 0$), the MEAs display comparable open-circuit voltages (OCV), indicating similar electrocatalytic activity at the triple-phase boundaries. However, as the galvanic load increases, divergent performance pathways emerge: MEA-3 maintains the highest cell potential across the ohmic-dominated regime, indicating minimized internal resistance and superior protonic conductivity. MEA-1 shows intermediate performance, while MEA-2 exhibits a more pronounced potential drop, particularly at elevated current densities ($j > 1.5$ A cm^{-2}). This divergence is highly pronounced in the high-current mass-transport-limited regime, where diffusion limitations and concentration overpotentials dominate. MEA-2 is highly susceptible to these transport limitations, as evidenced by its steep mass-transport polarization tail. Overall, MEA-3 demonstrates superior performance at 100% RH and 80 °C, achieving a peak power density (P_{max}) exceeding 0.75 W cm^{-2} (Figure 6B).

Figure 6C delineates the polarization profiles at a reduced hydration state of 65% RH. Under these moderately dry conditions, all three MEAs exhibit highly congruent $V-j$ behavior across the low-to-mid current-density ranges. Performance deviations become resolvable only at high current densities, where MEA-3 shows a marginal decline, indicative of local oxygen transport resistances or partial mass-transport limitations. Consequently, MEA-2 achieves the highest performance under 65% RH, reaching a peak power density of 0.72 W cm^{-2} (Figure 6D). Nevertheless,

21960216, 2026, 16, Downloaded from https://chemistry-europe.onlinelibrary.wiley.com/doi/10.1002/celc.70287 by Carlo Santoro - Area Sistemi Dipart & Doc , Wiley Online Library on [28/10/2026]. See the Terms and Conditions (https://onlinelibrary.wiley.com/terms-and-conditions) on Wiley Online Library for rules of use; OA articles are governed by the applicable Creative Commons License

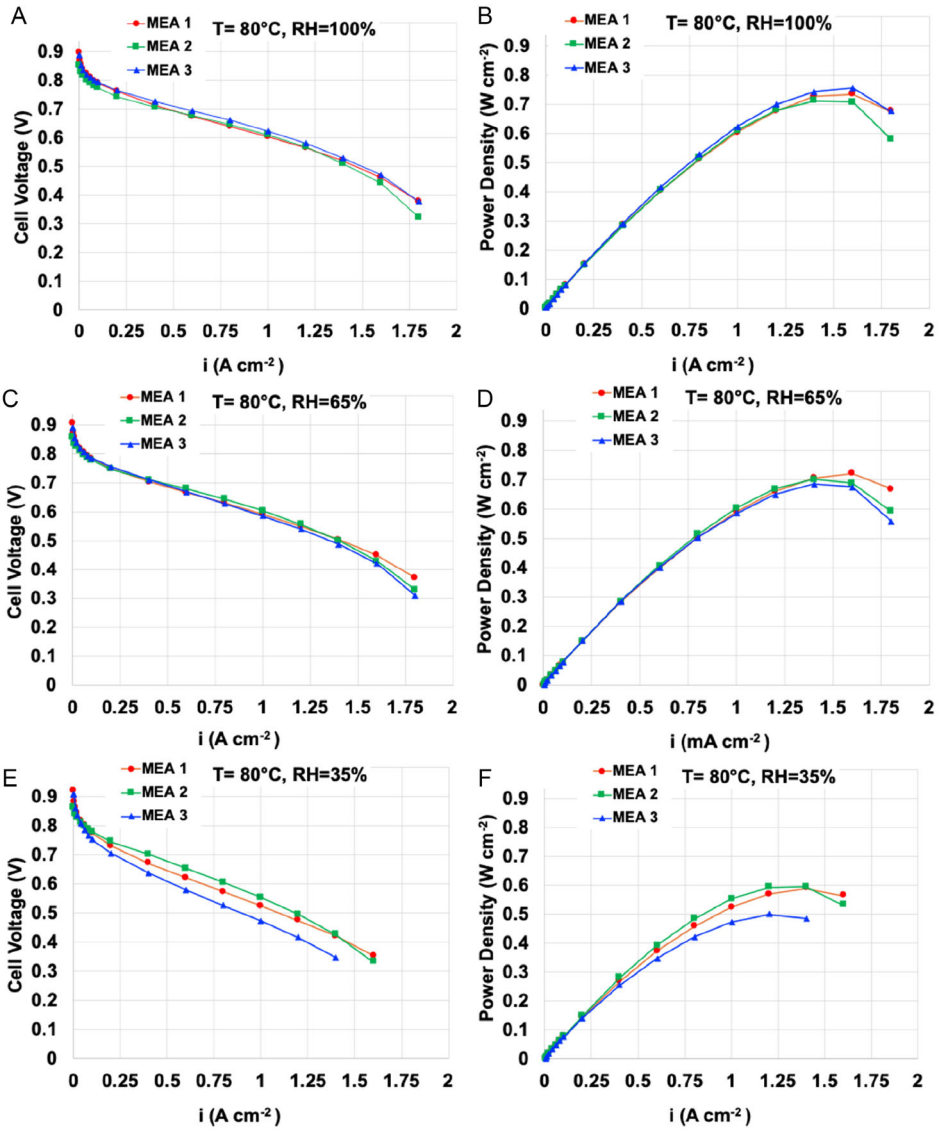


FIGURE 6 | Comparison of the polarization curves and power curves for all three MEAs investigated at (A) and (B) 80 °C and 100% relative humidity, (C) and (D) 80 °C and 65% relative humidity, and (E) and (F) 80 °C and 35% relative humidity.

the performance margins among all three MEAs are minimal, demonstrating robust and comparable charge-transport kinetics under partial humidification.

Figure 6E illustrates the electrochemical performance under dry operating conditions (35% RH). Under this low-humidity constraint, performance discrepancies among the MEAs are highly amplified. While low-load activation behaviors remain relatively uniform, the polarization curves diverge sharply under load. MEA-2 exhibits the highest performance, maintaining superior cell voltage across the entire current density range. This indicates that MEA-2 maintains lower ohmic resistance and enhanced hydration of its ionomer phase under low-humidity conditions. MEA-1 displays intermediate performance, whereas MEA-3 consistently records the poorest electrochemical response, exhibiting a severe voltage drop under high-load regimes. Consequently, MEA-3 yields the lowest peak power density under these dry conditions, measuring approximately 0.5 W cm^{-2} (Figure 6F).

The performance degradation of MEA-3 is primarily attributed to the structural characteristics of the EIG binder integrated into the cathode CL. Compared to the N+125D ionomer (790 g eq^{-1}, EW), the EIG binder possesses a significantly higher EW (1050 g eq^{-1}, EW). This elevated EW reduces the volumetric concentration of sulfonic acid sites, thereby decreasing the polymer's water uptake capacity and ionic conductivity (σ_{H^+}), which severely compromises proton transport kinetics. Consequently, while the EIG binder was utilized to lower local oxygen mass-transport resistance, it introduces a severe tradeoff in protonic conductivity, a drawback that is highly exacerbated under low RH conditions.

5.2 | CV

The CV profiles (Figure S10A) for MEA-1, MEA-2, and MEA-3 resolve the electrochemical surface area (ECSA) and the corresponding electrocatalytic activity of the respective cathode

21960216, 2026, 16, Downloaded from https://chemistry-europe.onlinelibrary.wiley.com/doi/10.1002/celc.70287 by Carlo Santoro - Area Sistemi Dipart & Doc , Wiley Online Library on [28/10/2026]. See the Terms and Conditions (https://onlinelibrary.wiley.com/terms-and-conditions) on Wiley Online Library for rules of use; OA articles are governed by the applicable Creative Commons License

CLs. The ECSA ($m^2 g_{Pt}^{-1}$) was quantitatively determined by integrating the charge associated with the hydrogen underpotential deposition (H_{upd}) adsorption/desorption region (0.05–0.40 V vs. RHE), assuming a charge density constant of 210 $\mu C\ cm_{Pt}^2$ for polycrystalline platinum. These values, alongside the calculated roughness factor (r.f.) and the cathodic Pt loadings, are summarized in Figure S10B. The r.f. is defined as the ratio of the active catalyst area to the geometrical surface area of the electrode. A higher r.f. typically results in increased current density during electrochemical reactions, as more active sites are available. For each MEA, the cathode r.f. was calculated by multiplying the ECSA by the platinum loading.

The calculated electrochemical metrics indicate that MEA-3 and MEA-1 exhibit the highest Pt-utilization efficiencies, yielding superior mass-specific ECSAs. Conversely, MEA-2 displays the lowest ECSA despite its high local Pt loading, indicating a significant fraction of electrocatalytically inactive or isolated Pt nanoparticles. Consequently, MEA-3 displays the most active catalyst–ionomer interface under fully saturated conditions, as evidenced by both its distinct H_{upd} features and quantitative diagnostics. However, despite possessing the highest intrinsic ECSA and r.f., the overall cell performance of MEA-3 suffers a severe decline under dry operating conditions. This degradation is driven by dominant ohmic overpotentials arising from elevated proton transport resistance within the high-EW EIG binder matrix. These results demonstrate that when utilizing alternative ionomers like EIG, optimizing the triple-phase boundary requires a careful tradeoff between local oxygen permeability and bulk protonic conductivity.

5.3 | EIS Analysis

EIS was utilized to deconvolute the individual contribution of activation, ohmic, and mass-transport overpotentials to the overall FC voltage loss. Measurements were systematically performed under the same RH regimes (100%, 65%, and 35% RH) at two diagnostic current densities: a low-load activation/ohmic-dominated regime (0.02 A cm^{-2}) and a high-load transport-limited regime (0.8 A cm^{-2}). The resulting Nyquist plots for MEA-1, MEA-2, and MEA-3 across the investigated operating envelope are compiled in Figure 7. The high-frequency intercept of the impedance arcs with the real axis (Z') yields the high-frequency resistance (HFR, R_{ohm}). This parameter represents the sum of the electronic contact resistances and the proton transport resistance of the membrane (R_{mem}). Because a baseline Nafion membrane of identical thickness was utilized across all MEAs, the R_{ohm} values remain virtually congruent under identical humidification levels.

The Nyquist profiles reveal a substantial reduction in the overall polarization resistance (R_p) when transitioning from low to high current density. Simultaneously, a distinct change in the spectra

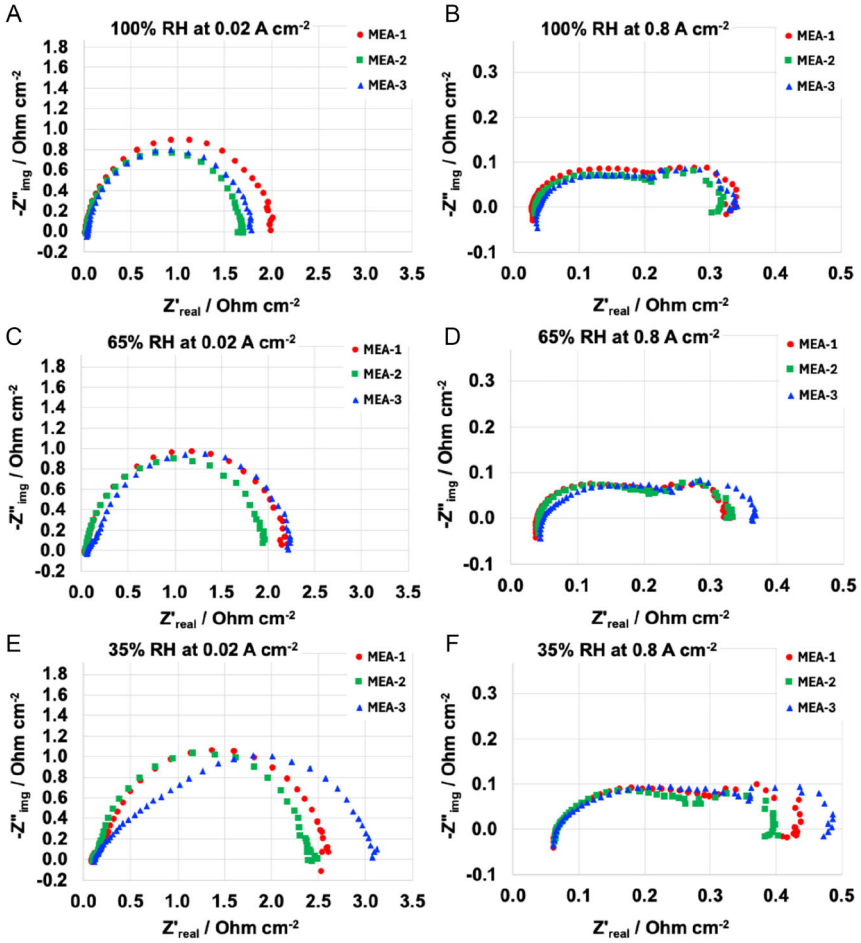


FIGURE 7 | Nyquist plots for all three MEAs at 0.02 A cm^{-2} (on the left) and 0.8 A cm^{-2} (on the right) with different relative humidity operations: (A) and (B) 100% RH, (C) and (D) 65% RH, and (E) and (F) 35% RH.

21960216, 2026, 16, Downloaded from https://chemistry-europe.onlinelibrary.wiley.com/doi/10.1002/celc.70287 by Carlo Santoro - Area Sistemi Dipart & Doc , Wiley Online Library on [28/10/2026]. See the Terms and Conditions (https://onlinelibrary.wiley.com/terms-and-conditions) on Wiley Online Library for rules of use; OA articles are governed by the applicable Creative Commons License

topology is observed: (i) At low current density (0.02 A cm^{-2}), the spectra display a single, broad charge-transfer loop, typical of a system dominated by the ORR activation kinetics (R_{ct}) at the cathode and (ii) at high current density (0.8 A cm^{-2}), the impedance spectra resolve into two distinct, overlapping capacitive loops. This high-load bimodal topology arises from the coupled contributions of charge–transfer kinetics (R_{ct}) in the high-to-mid frequency domain, and gas-phase or ionomeric mass-transport resistance (R_{mt}) in the low-frequency domain. The individual arc diameters quantify the magnitude of these discrete transport resistances.

Under fully humidified conditions (100% RH) at low current density (Figure 7A), MEA-2 exhibits a marginally smaller capacitive loop diameter compared to MEA-1 and MEA-3, indicating reduced activation resistance. Under these conditions, MEA-1 displays the largest arc diameter, correlating to the highest overall kinetic resistance. At high current density (Figure 7B), the total impedance arc collapses significantly for all samples, confirming a sharp reduction in R_{ct} due to enhanced electrochemical reaction rates. The variations among the three MEAs become highly muted under high-load saturated conditions, yielding comparable total polarization values. This convergence suggests that under maximum load at 100% RH, the dominant performance constraints shift from activation kinetics to bulk proton conduction and localized mass-transport limitations, which remain comparable across the three MEAs.

Under subsaturated conditions (<65% RH) and low current densities (J), MEA-1 exhibits a marginally smaller high-to-medium frequency capacitive loop (Nyquist arc) compared to MEA-2 and MEA-3. This indicates reduced charge-transfer (R_{ct}) and local mass-transport (R_{mt}) resistances under kinetically controlled conditions (Figure 7C). Notably, MEA-3 begins displaying a depressed, distorted capacitive loop under these conditions, a feature that becomes highly pronounced at lower RH. At high current density ($J = 0.8$ A cm^{-2}), the Nyquist plots of all MEAs converge, indicating that the systems operate in a regime dominated by bulk ohmic and oxygen-transport limitations. However, MEA-3 still presents a slightly elevated R_{ct} (Figure 7D). A unique impedance response is observed for MEA-3 at low current density under 35% RH (Figure 7E,F), where the high-frequency Nyquist arc shape deviates significantly from the other samples. Under these severely dehydrated conditions, the protonic conductivity of both the membrane and the CL ionomer is drastically reduced, making the ORR charge-transfer kinetics at the cathode as the rate-determining process. The expanded high-frequency arc diameter of MEA-3 indicates that its specific electrode morphology and hydration state induce a severe charge-transfer resistance, limiting performance at low J. This diagnostic behavior correlates directly with the poor in situ polarization performance observed for this MEA under identical operating conditions (Figure 6E). At higher loads, the capacitive arcs of all MEAs contract significantly—a classic manifestation of decreased activation impedance under high overpotentials. While the performance gap narrows, MEA-1 and MEA-2 maintain a smaller overall impedance envelope compared to MEA-3, confirming superior charge and mass transport kinetics under high load.

TABLE 4 | Proton-transport resistance (R_p) at each relative humidity condition for each MEA.

RH	30%	50%	90%	100%
Ionomer resistance	**Ohm cm^{-2}**			
MEA 1	0.667	0.207	0.033	0.017
MEA 2	0.403	0.14	0.019	0
MEA 3	4.467	0.857	0.185	0.125

To quantify local transport losses, the proton-transport resistance within the CL $R_{p,CL}$ was evaluated and summarized in Table 4.

The data reveal that the MEA utilizing the EIG binder (MEA-3) exhibits a significantly higher R_{CL}, particularly under low humidity (35% RH). This aligns with the polarization curves (Figure 6E), where MEA-3 displayed severe performance decay. The diminished protonic conductivity of EIG is attributed to its high EW relative to the benchmark N+125D ionomer. A higher EW corresponds to a lower ion exchange capacity (IEC), which restricts proton-hopping pathways. Conversely, MEA-2 demonstrated the lowest overall R_{CL}. Future work will go in the direction of optimization strategies for synthesizing lower-EW EIG polymers or formulating binary EIG/N+125D ionomer blends to synergize their respective physical stability and electrochemical transport properties.

5.4 | Limiting Current Measurements

Limiting current measurements can be used to evaluate oxygen mass-transport resistance (R_{O_2}). It is interesting to note that the MEA-1 shows an average R_{O_2} of 0.28 ± 0.03 s cm^{-1} (electrocatalyst loading 0.22 ± 0.02 mg cm^{-2}), MEA-2 has the highest average R_{O_2} value at 0.39 ± 0.08 s cm^{-1} (electrocatalyst loading 0.27 ± 0.02 mg cm^{-2}), and MEA-3 achieves the lowest average R_{O_2} value at 0.21 ± 0.01 s cm^{-2} (electrocatalyst loading 0.33 ± 0.02 mg cm^{-2}). These findings are particularly noteworthy as they confirm the advantageous role of the EIG binder in reducing oxygen resistance, thereby enhancing oxygen transport to the cathode electrocatalyst sites. Furthermore, it is important to highlight that cathode loading seems to have no impact on oxygen resistance, indicating that this may be influenced by the ionomer properties used as a binder in the electrode. Overall, the presence of EIG improves the efficiency of the ORR, a vital process in PEMFC operation. This enhancement helps minimize energy losses and can potentially extend the PEMFC operational lifespan.

5.5 | Polarization End of Life

To evaluate the electrochemical stability of the fabricated MEAs, postdiagnostic polarization curves were recorded at 80 °C following the impedance spectroscopy protocol. These end-of-life (EOL) polarization profiles were evaluated under fully humidified (100% RH), partially humidified (65% RH), and dehydrated (35% RH) conditions (Figure 8).

21960216, 2026, 16, Downloaded from https://chemistry-europe.onlinelibrary.wiley.com/doi/10.1002/celc.70287 by Carlo Santoro - Area Sistemi Dipart & Doc , Wiley Online Library on [28/10/2026]. See the Terms and Conditions (https://onlinelibrary.wiley.com/terms-and-conditions) on Wiley Online Library for rules of use; OA articles are governed by the applicable Creative Commons License

5.5.1 | *Fully Humidified Conditions (100% RH)*

Under fully saturated conditions (Figure 8A), the MEA-3 (utilizing the EIG cathode binder) demonstrated superior electrochemical stability at EOL compared to the other samples, achieving a peak power density (P_{max}) of 0.7 W cm^{-2} (Figure 8B). This indicates that the EIG binder successfully mitigates typical CL degradation mechanisms (e.g., carbon corrosion, ionomer washout, or platinum nanoparticle migration), preserving the active catalyst–ionomer interface. Particularly, MEA-1 displays intermediate EOL performance, with operational cell voltages (E_{cell}) consistently lower than MEA-3 but higher than MEA-2 across the entire current density (J) range. MEA-2 exhibits the most severe performance decay, particularly in the high-current-density region ($J > 1.0$ A cm^{-2}). This indicates substantial degradation of its electrode structure, likely driven by severe mass-transport limitations and increased ohmic losses.

The divergence of the polarization curves at elevated current densities highlights how AST-induced degradation differentially impacts the mass transport and ohmic resistance of each MEA. The enhanced EOL E_{cell} of MEA-3 under high-load conditions confirms its structural robustness, making it a highly viable candidate for heavy-duty applications where durability is paramount.

5.5.2 | *Partially Humidified Conditions (65% RH)*

Under subsaturated conditions (Figure 8C), the performance gap between the MEAs widens as a function of current density. In fact, MEA-3 consistently delivers the highest E_{cell} across all current densities, demonstrating superior retention of both ECSA and proton conductivity under moderate dehydration. In parallel, MEA-1 exhibits intermediate durability, with polarization curves tracking slightly below MEA-3. MEA-2 suffers severe degradation, characterized by a sharp voltage drop at high J. This is indicative of accelerated aging, potentially due to severe ionomer degradation or collapse of the CL pore structure, which exacerbates oxygen transport resistance.

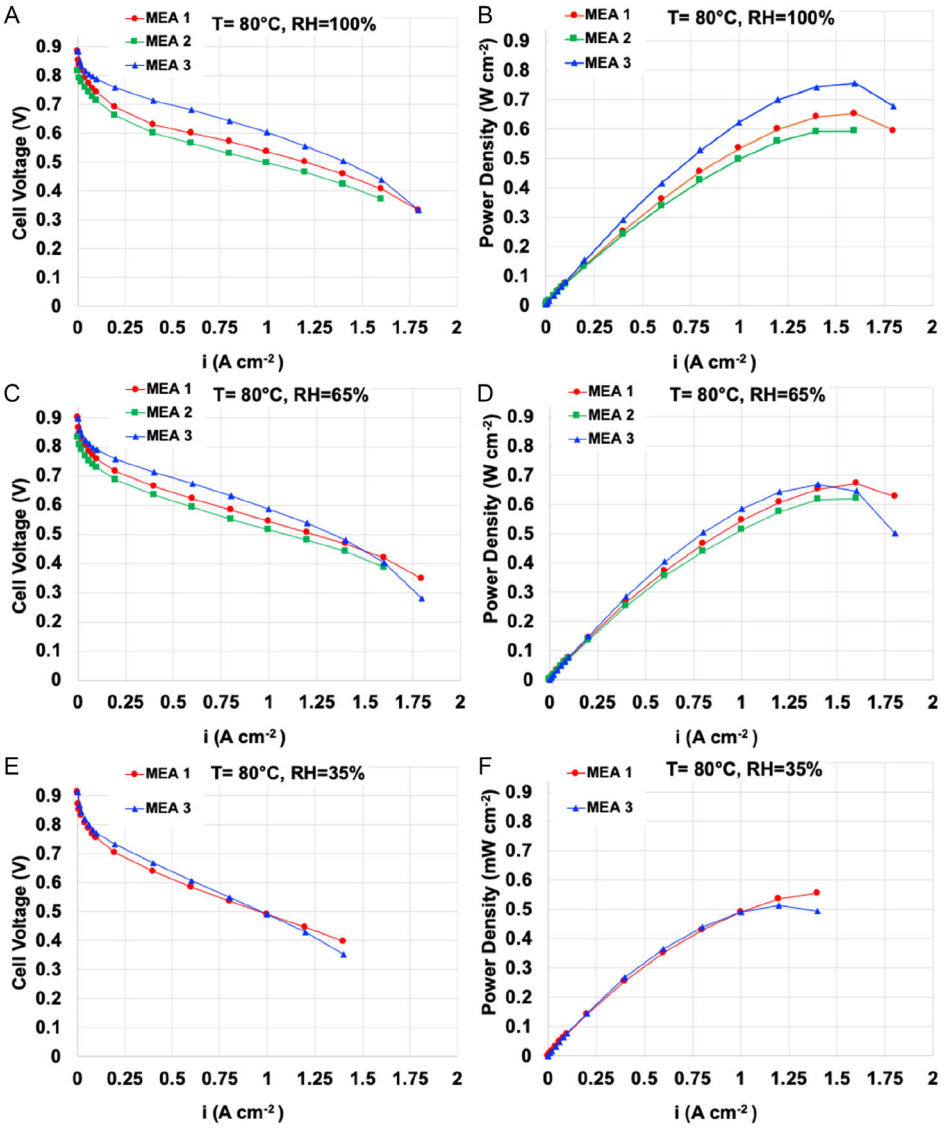


FIGURE 8 | Comparison of the polarization curves and power curves for all three MEAs investigated at (A) and (B) 80 °C and 100% relative humidity, (C) and (D) 80 °C and 65% relative humidity, and (E) and (F) 80 °C and 35% relative humidity at the end of their life (EOL).

21960216, 2026, 16, Downloaded from https://chemistry-europe.onlinelibrary.wiley.com/doi/10.1002/celc.70287 by Carlo Santoro - Area Sistemi Dipart & Doc , Wiley Online Library on [28/10/2026]. See the Terms and Conditions (https://onlinelibrary.wiley.com/terms-and-conditions) on Wiley Online Library for rules of use; OA articles are governed by the applicable Creative Commons License

5.5.3 | *Dehydrated Conditions (35% RH)*

Under severe low-humidity conditions (Figure 8E), the EOL polarization curve of MEA-2 is omitted due to important performance loss. A direct comparison between MEA-1 and MEA-3 reveals distinct operating regimes. In the activation regime (low J), MEA-3 exhibits a slightly higher E_{cell} compared to MEA-1, indicating superior kinetic retention of the ORR active sites in the EIG-based CL. In the ohmic/mass-transport regime (high J), a distinct crossover occurs. At high load, MEA-1 outperforms MEA-3, which experiences a more pronounced mass transport/ohmic polarization drop. This is also reflected in the EOL power-density profiles (Figure 8F).

This behavior suggests that while the EIG binder in MEA-3 provides superior kinetic protection, it remains susceptible to localized proton-transport resistance or liquid-water management issues under demanding, dry operating conditions. Nonetheless, both MEAs exhibit comparable overall durability profiles under these extreme testing parameters.

6 | Conclusions

This research provides a comprehensive analysis of the electrochemical performance of various MEA configurations, each developed using different ionomers and electrode preparation methods. Specifically, two polymers were examined: a SSC ionomer (N+125D, EW = 790) and a HOPI (EIG, EW = 1050) as binder into a Pt/C electrode. The goal was to optimize the CL microstructure and enhance overall electrochemical performance.

Two electrodes containing N+125D were prepared using different methods: one with a water/alcohol ratio of 50:50 and the other with a ratio of 25:75. The preparation process for the 25:75 composition required further optimization. In contrast, due to the properties of EIG, the electrode was prepared using only a water/alcohol ratio of 50:50. All three inks were used in preparing electrodes E-1 and E-2, which are based on the N+125D ionomer and formulated with 1-propanol at water/1-propanol ratios of 50:50 and 25:75, respectively. Electrode E-3 was prepared using EIG.

All electrodes were used to prepare three MEAs: one based entirely on E-1, another on E-2, and a third with E-3 as the cathode and E-1 as the anode. In each MEA, an Aquivion-reinforced membrane (EW 720) was used as the electrolyte.

The results clearly demonstrate that MEA-3 is the most promising configuration among those evaluated. It offers both high initial performance and excellent EOL stability, with significantly lower oxygen resistance than the other MEAs. The optimized structure of the EIG ionomer in MEA-3 improves reactant transport to the catalytic sites and minimizes diffusional losses, resulting in greater overall FC efficiency and polarization curves with superior performance. Even at EOL, MEA-3 preserved much of its initial performance, exhibiting only a moderate voltage drop and strong resistance to degradation.

In comparison, MEA-1 showed intermediate performance, while MEA-2, despite a competitive start, experienced more severe degradation, likely due to higher impedance and less efficient catalyst utilization. MEA-3 had the highest ECSA and roughness factor, indicating more accessible catalytic sites and better platinum utilization. In contrast, MEA-2 had the lowest ECSA, reflecting limited intrinsic catalytic activity.

It is important to note, however, that MEA-3 was more sensitive to humidity. While it performed exceptionally well under high RH, its performance declined significantly under dry conditions. This is mainly due to the lower water-retention capacity of the EIG ionomer compared to N+125D, which can be explained by its higher EW of 1050 vs. 790 for N+125D.

The findings of this study demonstrate that incorporating EIG into electrode fabrication can significantly improve electrochemical performance compared to conventional SSC polymers. These enhancements are mainly due to increased oxygen transport within the CL, which supports more efficient ORRs and overall FC performance.

Acknowledgments

The paper was corrected in terms of typos, mistakes, colloquial forms, nontechnical sentences and so on with the support of Google Gemini. This work received funding from the Italian government (Ministero dell'Ambiente e della Sicurezza Energetica), under the program Progetto Permanent - Bando MITE PNRR Missione 2 Investimento 3.5 A - RSH2A_0O0012.

Open access publishing facilitated by Universita degli Studi di Milano-Bicocca, as part of the Wiley - CRUI-CARE agreement.

Conflicts of Interest

The authors declare no conflicts of interest.

Data Availability Statement

The data that support the findings of this study are available from the corresponding author upon reasonable request.

References

1. S. Mo, L. Du, Z. Huang, et al., "Recent Advances on PEM Fuel Cells: From Key Materials to Membrane Electrode Assembly," *Electrochemical Energy Reviews* 6 (2023): 28, https://doi.org/10.1007/s41918-023-00190-w.

2. M. Tawalbeh, S. Alarab, A. Al-Othman, and R. M. N. Javed, "The Operating Parameters, Structural Composition, and Fuel Sustainability Aspects of PEM Fuel Cells: A Mini Review," *Fuels* 3, no. 3 (2022): 449–474, https://doi.org/10.3390/fuels3030028.

3. F. Zhang, B. Zu, B. Wang, et al., "Developing Long-Durability Proton-Exchange Membrane Fuel Cells," *Joule* 9 (2025): 101853, https://doi.org/10.1016/j.joule.2025.101853.

4. J.-H. Kim, M. S. Noh, E. J. Shin, et al., "Improved Mechanical Stability and Proton Conductivity of Reinforced Membranes for Proton Exchange Membrane Fuel Cells (PEMFCs)," *ACS Physical Chemistry Au* 5 (2025): 425–434, https://doi.org/10.1021/acsphyschemau.5c00009.

5. A. Parekh, "Recent Developments of Proton Exchange Membranes for PEMFC: A Review," *Frontiers in Energy Research* 10 (2022): 956132, https://doi.org/10.3389/fenrg.2022.956132.

6. H. Qiao, M. Zhang, J. Che, et al., "Recent Advances of Hydrogen Oxidation: Reaction Mechanism, Catalytic Activity Enhancement, and

21960216, 2026, 16, Downloaded from https://chemistry-europe.onlinelibrary.wiley.com/doi/10.1002/celc.70287 by Carlo Santoro - Area Sistemi Dipart & Doc , Wiley Online Library on [28/10/2026]. See the Terms and Conditions (https://onlinelibrary.wiley.com/terms-and-conditions) on Wiley Online Library for rules of use; OA articles are governed by the applicable Creative Commons License

Applications," *International Journal of Hydrogen Energy* 201 (2026): 152978, https://doi.org/10.1016/j.ijhydene.2025.152978.

7. S. Park, E. Lee, Y. Park, M.-G. Kim, and S. J. Yoo, "Toward Hydrogen Mobility: Challenges and Strategies in Electrocatalyst Durability for Long-Term PEMFC Operation," *JACS Au* 5 (2025): 1617–1632, https://doi.org/10.1021/jacsau.5c00173.

8. M. Janssen, P. Weber, and M. Oezaslan, "Recent Advances of Various Pt-Based Catalysts for Oxygen Reduction Reaction (ORR) in Polymer Electrolyte Membrane Fuel Cells (PEMFCs)," *Current Opinion in Electrochemistry* 40 (2023): 101337, https://doi.org/10.1016/j.coelec.2023.101337.

9. J. D. Sinniah, W. Y. Wong, K. S. Loh, R. M. Yunus, and S. N. Timmiati, "Perspectives on Carbon-Alternative Materials as Pt Catalyst Supports for a Durable Oxygen Reduction Reaction in Proton Exchange Membrane Fuel Cells," *Journal of Power Sources* 534 (2022): 231422, https://doi.org/10.1016/j.jpowsour.2022.231422.

10. X. X. Wang, J. Sokolowski, H. Liu, and G. Wu, "Pt Alloy Oxygen-Reduction Electrocatalysts: Synthesis, Structure, and Property," *Chinese Journal of Catalysis* 41 (2020): 739–755, https://doi.org/10.1016/S1872-2067(19)63407-8.

11. L. Huang, S. Zaman, X. Tian, Z. Wang, W. Fang, and B. Y. Xia, "Advanced Platinum-Based Oxygen Reduction Electrocatalysts for Fuel Cells," *Accounts of Chemical Research* 54 (2021): 311–322, https://doi.org/10.1021/acs.accounts.0c00488.

12. S. Kolluru, G. M. Jain, D. Gollapudi, L. E. Reddy, and G. V. Ramesh, "Recent Developments in Pt-Based Alloy Nanoparticles for Oxygen Reduction Reaction in Fuel Cells," *Materials Today: Proceedings* 92 (2023): 764–770, https://doi.org/10.1016/j.matpr.2023.04.320.

13. H. Ren, X. Meng, Y. Lin, and Z. Shao, "Structural Stability of Catalyst Ink and Its Effects on the Catalyst Layer Microstructure and Fuel Cell Performance," *Journal of Power Sources* 517 (2022): 230698, https://doi.org/10.1016/j.jpowsour.2021.230698.

14. H. Ren, X. Meng, Y. Lin, and Z. Shao, "Microstructure Formation Mechanism of Catalyst Layer and Its Effect on Fuel Cell Performance: Effect of Dispersion Medium Composition," *Journal of Energy Chemistry* 73 (2022): 588–598, https://doi.org/10.1016/j.jechem.2022.06.034.

15. J. Fan, M. Chen, Z. Zhao, et al., "Bridging the Gap Between Highly Active Oxygen Reduction Reaction Catalysts and Effective Catalyst Layers for Proton Exchange Membrane Fuel Cells," *Nature Energy* 6 (2021): 475–486, https://doi.org/10.1038/s41560-021-00824-7.

16. H. Ren, Y. Teng, X. Meng, et al., "Ionomer Network of Catalyst Layers for Proton Exchange Membrane Fuel Cell," *Journal of Power Sources* 506 (2021): 230186, https://doi.org/10.1016/j.jpowsour.2021.230186.

17. T. Maiyalagan and S. Pasupathi, "Components for PEM Fuel Cells: An Overview," *Materials Science Forum* 657 (2010): 143–189, https://doi.org/10.4028/www.scientific.net/MSF.657.143.

18. X. Shangguan, Y. Li, Y. Qin, S. Cao, J. Zhang, and Y. Yin, "Effect of the Porosity Distribution on the Liquid Water Transport in the Gas Diffusion Layer of PEMFC," *Electrochimica Acta* 371 (2021): 137814, https://doi.org/10.1016/j.electacta.2021.137814.

19. P. C. Okonkwo and C. Otor, "A Review of Gas Diffusion Layer Properties and Water Management in Proton Exchange Membrane Fuel Cell System," *International Journal of Energy Research* 45 (2021): 3780–3800, https://doi.org/10.1002/er.6227.

20. S. Woo, S. Lee, A. Z. Taning, T.-H. Yang, S.-H. Park, and S.-D. Yim, "Current Understanding of Catalyst/Ionomer Interfacial Structure and Phenomena Affecting the Oxygen Reduction Reaction in Cathode Catalyst Layers of Proton Exchange Membrane Fuel Cells," *Current Opinion in Electrochemistry* 21 (2020): 289–296, https://doi.org/10.1016/j.coelec.2020.03.006.

21. M. Uchida, "PEFC Catalyst Layers: Effect of Support Microstructure on Both Distributions of Pt and Ionomer and Cell Performance and Durability," *Current Opinion in Electrochemistry* 21 (2020): 209–218, https://doi.org/10.1016/j.coelec.2020.02.019.

22. Y. Guo, F. Pan, W. Chen, et al., "The Controllable Design of Catalyst Inks to Enhance PEMFC Performance: A Review," *Electrochemical Energy Reviews* 4 (2021): 67–100, https://doi.org/10.1007/s41918-020-00083-2.

23. W. Yu, F. Luo, X. Liang, et al., "Ionomeric Binders in Polymer Electrolyte Fuel Cells: Roles, Challenges, and Advances," *Chemical Society Reviews* 54 (2025): 9407–9456, https://doi.org/10.1039/D5CS00406C.

24. X. Yan, Z. Xu, S. Yuan, et al., "Structural and Transport Properties of Ultrathin Perfluorosulfonic Acid Ionomer Film in Proton Exchange Membrane Fuel Cell Catalyst Layer: A Review," *Journal of Power Sources* 536 (2022): 231523, https://doi.org/10.1016/j.jpowsour.2022.231523.

25. H. Eskandari, D. K. Paul, A. P. Young, and K. Karan, "Humidity-Dependent Hydration and Proton Conductivity of PFSA Ionomer Thin Films at Fuel-Cell-Relevant Temperatures: Effect of Ionomer Equivalent Weight and Side-Chain Characteristics," *ACS Applied Materials & Interfaces* 14 (2022): 50762–50772, https://doi.org/10.1021/acsami.2c12667.

26. X.-Z. Yuan, C. Nayoze-Coynel, N. Shaigan, et al., "A Review of Functions, Attributes, Properties and Measurements for the Quality Control of Proton Exchange Membrane Fuel Cell Components," *Journal of Power Sources* 491 (2021): 229540, https://doi.org/10.1016/j.jpowsour.2021.229540.

27. N. Ramaswamy, S. Kumaraguru, R. Koestner, et al., "Editors' Choice—Ionomer Side Chain Length and Equivalent Weight Impact on High Current Density Transport Resistances in PEMFC Cathodes," *Journal of the Electrochemical Society* 168 (2021): 024518, https://doi.org/10.1149/1945-7111/abe5eb.

28. T. Li, J. Shen, G. Chen, S. Guo, and G. Xie, "Performance Comparison of Proton Exchange Membrane Fuel Cells With Nafion and Aquivion Perfluorosulfonic Acids With Different Equivalent Weights as the Electrode Binders," *ACS Omega* 5 (2020): 17628–17636, https://doi.org/10.1021/acsomega.0c02110.

29. G. M. Carrabba, E. Sartoretti, E. Parisi, E. Simone, and A. H. A. Monteverde, "Carbon Corrosion Resistance in PEM Fuel Cells: Comparative Study of Short and Long Side Chain Perfluorosulfonic Acid Ionomers," *International Journal of Hydrogen Energy* 133 (2025): 546–559, https://doi.org/10.1016/j.ijhydene.2025.04.262.

30. N. Zhao, Z. Shi, and F. Girard, "Superior Proton Exchange Membrane Fuel Cell (PEMFC) Performance Using Short-Side-Chain Perfluorosulfonic Acid (PFSA) Membrane and Ionomer," *Materials* 15 (2022): 78, https://doi.org/10.3390/ma15010078.

31. I. Gatto, A. Saccà, D. Sebastián, et al., "Influence of Ionomer Content in the Catalytic Layer of MEAs Based on Aquivion Ionomer," *Polymers* 13 (2021): 3832, https://doi.org/10.3390/polym13213832.

32. K. D. Kreuer, M. Schuster, B. Obliers, et al., "Short-Side-Chain Proton Conducting Perfluorosulfonic Acid Ionomers: Why They Perform Better in PEM Fuel Cells," *Journal of Power Sources* 178 (2008): 499–509, https://doi.org/10.1016/j.jpowsour.2007.11.011.

33. Y. Prykhodko, K. Fatyeyeva, L. Hespel, and S. Marais, "Progress in Hybrid Composite Nafion-Based Membranes for Proton Exchange Fuel Cell Application," *Chemical Engineering Journal* 409 (2021): 127329, https://doi.org/10.1016/j.cej.2020.127329.

34. C. Chen and T. F. Fuller, "The Effect of Humidity on the Degradation of Nafion Membrane," *Polymer Degradation and Stability* 94 (2009): 1436–1447, https://doi.org/10.1016/j.polymdegradstab.2009.05.016.

35. H. Wang, R. Wang, S. Sui, T. Sun, Y. Yan, and S. Du, "Cathode Design for Proton Exchange Membrane Fuel Cells in Automotive Applications," *Automotive Innovation* 4 (2021): 144–164, https://doi.org/10.1007/s42154-021-00148-y.

21960216, 2026, 16, Downloaded from https://chemistry-europe.onlinelibrary.wiley.com/doi/10.1002/celc.70287 by Carlo Santoro - Area Sistemi Dipart & Doc , Wiley Online Library on [28/10/2026]. See the Terms and Conditions (https://onlinelibrary.wiley.com/terms-and-conditions) on Wiley Online Library for rules of use; OA articles are governed by the applicable Creative Commons License

36. Y. Li, Z. Wu, C. Wang, et al., "Engineering Triple-Phase Boundary in Pt Catalyst Layers for Proton Exchange Membrane Fuel Cells," *Advanced Functional Materials* 34 (2024): 2310428, https://doi.org/10.1002/adfm.202310428.

37. Q. Meyer, S. Liu, K. Ching, Y. D. Wang, and C. Zhao, "Operando Monitoring of the Evolution of Triple-Phase Boundaries in Proton Exchange Membrane Fuel Cells," *Journal of Power Sources* 557 (2023): 232539, https://doi.org/10.1016/j.jpowsour.2022.232539.

38. Y. Yao, X. Zhang, L. Xu, et al., "Ouyang, Investigation of the Mechanism of Local Oxygen Transport Resistance at the Triple Phase Boundary Regulated by Ionomer Content: Experiment and Agglomerate Modeling," *Journal of Power Sources* 667 (2026): 239234, https://doi.org/10.1016/j.jpowsour.2025.239234.

39. M. Chen, C. Zhao, F. Sun, J. Fan, H. Li, and H. Wang, "Research Progress of Catalyst Layer and Interlayer Interface Structures in Membrane Electrode Assembly (MEA) for Proton Exchange Membrane Fuel Cell (PEMFC) System," *eTransportation* 5 (2020): 100075, https://doi.org/10.1016/j.etran.2020.100075.

40. J. Zhao, H. Liu, and X. Li, "Structure, Property, and Performance of Catalyst Layers in Proton Exchange Membrane Fuel Cells," *Electrochemical Energy Reviews* 6 (2023): 13, https://doi.org/10.1007/s41918-022-00175-1.

41. Y. Sun, S. Polani, F. Luo, S. Ott, P. Strasser, and F. Dionigi, "Advancements in Cathode Catalyst and Cathode Layer Design for Proton Exchange Membrane Fuel Cells," *Nature Communications* 12 (2021): 5984, https://doi.org/10.1038/s41467-021-25911-x.

42. S. Mehrazi, M. Sarker, F. Mojica, P. Rolfe, and P.-Y. A. Chuang, "A Rheological Approach to Studying Process-Induced Structural Evolution of the Microporous Layer in a Proton Exchange Membrane Fuel Cell," *Electrochimica Acta* 389 (2021): 138690, https://doi.org/10.1016/j.electacta.2021.138690.

43. S. Du, W. Li, H. Wu, P.-Y. A. Chuang, M. Pan, and P.-C. Sui, "Effects of Ionomer and Dispersion Methods on Rheological Behavior of Proton Exchange Membrane Fuel Cell Catalyst Layer Ink," *International Journal of Hydrogen Energy* 45 (2020): 29430–29441, https://doi.org/10.1016/j.ijhydene.2020.07.241.

44. P. Lauf, V. Lloret, M. Geuß, et al., "Characterization of Oxygen and Ion Mass Transport Resistance in Fuel Cell Catalyst Layers in Gas Diffusion Electrode Setups," *Journal of the Electrochemical Society* 170 (2023): 064509, -https://doi.org/10.1149/1945-7111/acdafb.

45. T. Reshetenko and B. L. Ben, "I'mpact of a Gas Diffusion Layer's Structural and Textural Properties on Oxygen Mass Transport Resistance in the Cathode and Performance of Proton Exchange Membrane Fuel Cells," *Electrochimica Acta* 371 (2021): 137752, https://doi.org/10.1016/j.electacta.2021.137752.

46. D. Yang, Y. Guo, H. Tang, et al., "Influence of the Dispersion State of Ionomer on the Dispersion of Catalyst Ink and the Construction of Catalyst Layer," *International Journal of Hydrogen Energy* 46 (2021): 33300–33313, https://doi.org/10.1016/j.ijhydene.2021.07.172.

47. C. Li, K. Yu, A. Bird, et al., "Unraveling the Core of Fuel Cell Performance: Engineering the Ionomer/Catalyst Interface," *Energy & Environmental Science* 16 (2023): 2977–2990, https://doi.org/10.1039/d2ee03553g.

48. R. Jinnouchi, K. Kudo, K. Kodama, et al., "The Role of Oxygen-Permeable Ionomer for Polymer Electrolyte Fuel Cells," *Nature Communications* 12 (2021): 4956, https://doi.org/10.1038/s41467-021-25301-3.

49. M. Tempelaere, M. Zimmermann, and M. Chatenet, "3D-Structured Electrocatalysts for Improved Mass-Transfer in Proton-Exchange Membrane Fuel Cell Cathodes," *Current Opinion in Electrochemistry* 41 (2023): 101353, https://doi.org/10.1016/j.coelec.2023.101353.

50. J. P. Braaten, N. N. Kariuki, D. J. Myers, et al., "Integration of a High Oxygen Permeability Ionomer Into Polymer Electrolyte Membrane Fuel Cell Cathodes for High Efficiency and Power Density," *Journal of Power Sources* 522 (2022): 230821, https://doi.org/10.1016/j.jpowsour.2021.230821.

51. A. Rolfi, C. Oldani, L. Merlo, D. Facchi, and R. Ruffo, "New Perfluorinated Ionomer With Improved Oxygen Permeability for Application in Cathode Polymeric Electrolyte Membrane Fuel Cell," *Journal of Power Sources* 396 (2018): 95–101, https://doi.org/10.1016/j.jpowsour.2018.05.093.

52. T. A. Greszler, D. Caulk, and P. Sinha, "The Impact of Platinum Loading on Oxygen Transport Resistance," *Journal of the Electrochemical Society* 159 (2012): F831, https://doi.org/10.1149/2.061212jes.

53. X. Wang, X. Z. Yuan and H. Li, *PEM Fuel Cell Diagnostic Tools*, (CRC Press, 2012).

54. D. R. Baker, D. A. Caulk, K. C. Neyerlin, and M. W. Murphy, "Measurement of Oxygen Transport Resistance in PEM Fuel Cells by Limiting Current Methods," *Journal of the Electrochemical Society* 156 (2009): B991, https://doi.org/10.1149/1.3152226.

55. S. Bapat, C. Giehl, S. Kohsakowski, V. Peinecke, M. Schäffler, and D. Segets, "On the State and Stability of Fuel Cell Catalyst Inks," *Advanced Powder Technology* 32 (2021): 3845–3859, https://doi.org/10.1016/j.apt.2021.08.030.

56. J. Santana, M. Espinoza, T. S. Li, and M. Andersson, "A Detailed Analysis of Internal Resistance of a PEFC Comparing High and Low Humidification of the Reactant Gases," *Frontiers in Energy Research* 8 (2020): 217, https://doi.org/10.3389/fenrg.2020.00217.

57. Y. Yu, H. Li, H. Wang, X. Z. Yuan, G. Wang, and M. Pan, "A Review on Performance Degradation of Proton Exchange Membrane Fuel Cells During Startup and Shutdown Processes: Causes, Consequences, and Mitigation Strategies," *Journal of Power Sources* 205 (2012): 10–23, https://doi.org/10.1016/j.jpowsour.2012.01.059.

Supporting Information

Additional supporting information can be found online in the Supporting Information section.

21960216, 2026, 16, Downloaded from https://chemistry-europe.onlinelibrary.wiley.com/doi/10.1002/celc.70287 by Carlo Santoro - Area Sistemi Dipart & Doc , Wiley Online Library on [28/10/2026]. See the Terms and Conditions (https://onlinelibrary.wiley.com/terms-and-conditions) on Wiley Online Library for rules of use; OA articles are governed by the applicable Creative Commons License